The effect of liquid composition on the partitioning of Ni between olivine and silicate melt.

Andrew K. Matzen[1,2*]

Michael B. Baker[1]

John R. Beckett[1]

Bernard J. Wood[2]

Edward M. Stolper[1]

[*] Corresponding author. Present address: Department of Earth Sciences, University of Oxford, UK, OX1 3AN. Email: andrew.matzen@earth.ox.ac.uk, Telephone: +44 (0)1865 272026, Fax: +44 (0)1865 272072

[1] California Institute of Technology, Pasadena, CA 91125

[2] Department of Earth Sciences, University of Oxford, UK, OX1 3AN

For submission to Contributions to Mineralogy and Petrology

Abstract

We report the results of experiments designed to separate the effects of temperature and pressure from liquid composition on the partitioning of Ni between olivine and liquid, $D_{Ni}^{ol/liq}$. Experiments were performed from 1300–1600°C and 1-atm–3.0 GPa, using mid-ocean ridge basalt (MORB) glass surrounded by powdered olivine in graphite-Pt double capsules at high pressure, and powdered MORB in crucibles fabricated from single crystals of San Carlos olivine at one atmosphere. In these experiments, pressure and temperature were varied in such a way that we produced a series of liquids, each with an approximately constant composition (~12, ~15, and ~21 wt. % MgO). Previously, we used a similar approach to show that $D_{Ni}^{ol/liq}$ for a liquid with ~18 wt. % MgO is a strong function of temperature. Combining the new data presented here with our previous results allows us to separate the effects of temperature from composition.

We fit our data based on a Ni-Mg exchange reaction, which yields $\ln\left(D_{Ni}^{molar}\right) = \frac{-\Delta_r H^{\circ}_{T_{ref},P_{ref}}}{RT} + \frac{\Delta_r S^{\circ}_{T_{ref},P_{ref}}}{R} - \ln\left(\frac{X_{MgO}^{liq}}{X_{MgSi_{0.5}O_2}^{ol}}\right)$. Each subset of constant composition experiments displays roughly the same temperature dependence of $D_{Ni}^{ol/liq}$(i.e., $-\Delta_r H^{\circ}_{T_{ref},P_{ref}} \big/ R$) as previously reported for liquids with ~18 wt. % MgO. Fitting new data presented here (15 experiments) in conjunction with our 13 previously published experiments (those with ~18 wt. % MgO in the silicate liquid) to the above expression gives $\frac{-\Delta_r H^{\circ}_{T_{ref},P_{ref}}}{R}$ = 3,641 ± 396 (K) and $\Delta_{r(1)} S^{\circ}_{T_{ref},P_{ref}} \big/ R = -1.597 \pm 0.229$. Adding data from the literature yields $-\Delta_{r(1)} H^{\circ}_{T_{ref},P_{ref}} \big/ R$ = 4,505 ± 196 (K) and $\Delta_{r(1)} S^{\circ}_{T_{ref},P_{ref}} \big/ R = -2.075 \pm 0.120$, a set of coefficients that leads to a predictive equation for $D_{Ni}^{ol/liq}$ applicable to a wide range of melt compositions.

We use the results of our work to model the melting of peridotite beneath lithosphere of varying thickness, and show that: (1), a positive correlation between NiO in magnesian olivine phenocrysts and lithospheric thickness is expected given a temperature dependent $D_{Ni}^{ol/liq}$, and (2), the magnitude of the slope for natural samples is consistent with our experimentally determined temperature dependence. Alternative processes to generate the positive correlation between NiO in magnesian olivines and lithospheric thickness, such as the melting of olivine-free pyroxenite, are possible but they are not required to explain the observed correlation of NiO concentration in initially crystallizing olivine with lithospheric thickness.

Keywords: Nickel partitioning; olivine; Hawaii; Iceland; ocean-island basalt

Introduction

Unlike most other minor and trace elements, Ni is compatible in olivine (ol) over a broad range of temperatures, pressures, and silicate liquid (liq) compositions (i.e., $D_{Ni}^{ol/liq}$= NiO^{ol}/NiO^{liq} is greater than one, where NiO$^{\varphi}$ refers to the concentration of NiO in phase φ by weight). One consequence of the compatibility of Ni in olivine and other mantle phases (e.g., Mysen 1978) is that the NiO contents of residual lherzolites are insensitive to low degrees of partial melting; this is consistent with the observed narrow distribution of the NiO contents of olivines from spinel lherzolites: 0.37 (median) ± 0.03 [mean absolute deviation (MAD)], 308 analyses (Korenaga and Kelemen 2000; Korenaga personal communication 2011) and 0.37 ± 0.01, 172 analyses (Herzberg et al. 2013). Thus, unless the degree of melting is very high (e.g., >50%; Herzberg et al. 2016), one might reasonably expect that the first olivines to crystallize from a partial melt of a lherzolitic source would recover, within ~8%, the NiO content of olivine in the initially unmelted source (Herzberg et al. 2016). However, olivine phenocrysts from ocean islands often have NiO contents exceeding 0.5 wt. % (e.g., Clague et al. 1991; Sobolev et al. 2005; Sobolev et al. 2007). Possible explanations for these elevated NiO concentrations in olivine—and the melts from which they are derived—include an olivine-free component in the mantle produced by metasomatism of peridotite by silicic partial melts of recycled oceanic crust (Sobolev et al. 2005; Sobolev et al. 2007), Ni-enrichment in the mantle source due to interaction with the Ni-rich core (Ryabchikov 2003; Herzberg et al. 2013), or a $D_{Ni}^{ol/liq}$ that is a function of temperature (T) and/or pressure (P), in addition to composition (Leeman and Lindstrom 1978; Mysen and Kushiro 1979; Li and Ripley 2010; Putirka et al. 2011; Matzen et al. 2013).

Our ability to discriminate among these hypotheses depends on knowing $D_{Ni}^{ol/liq}$ and, specifically, how $D_{Ni}^{ol/liq}$ is affected by variables such as temperature, pressure, oxygen fugacity

($f\mathrm{O}_2$), and olivine and liquid compositions. Experiments in most studies measuring $D_{Ni}^{ol/liq}$ for a given bulk composition have been performed at a single pressure; thus, any change in temperature results in a change in liquid composition as olivine is added or subtracted from the liquid. Interpreting the results of such experiments is not straightforward because changes in liquid composition, olivine composition, and temperature, or a combination of these factors could result in the observed changes in $D_{Ni}^{ol/liq}$ (Arndt 1977; Hart and Davis 1978; Takahashi 1978; Wang and Gaetani 2008; Putirka et al. 2011). Matzen et al. (2013) isolated the effects of pressure and temperature from those of composition by performing experiments in which pressure and temperature were changed in concert; this yielded coexisting olivine-liquid pairs with roughly constant olivine Mg#s (100×Mg/[Mg+Fe], molar) of ~90, which we refer to as Fo_{90}, and liquid compositions of ~18 wt. % MgO. These experiments showed for a picritic liquid, that temperature has a significant effect on $D_{Ni}^{ol/liq}$. Here, we present the results of similar series of experiments designed to determine if the temperature dependence of $D_{Ni}^{ol/liq}$ is also a significant function of liquid composition, as predicted by Hirschmann and Ghiorso (1994).

Experimental and Analytical Methods

Run conditions are given in Table 1 and shown graphically in Fig. 1a. We used the same experimental methods and materials as Matzen et al. (2013; see their Table 1 for a description of starting materials). Briefly, we performed high-pressure experiments by surrounding a small chip of fused Juan de Fuca MORB glass with powdered Kilbourne Hole olivine in a Pt–graphite double capsule. Experiments were run in two stages: (1) a filled capsule was sintered at a temperature below the estimated solidus of the basalt [based on the Pertermann and Hirschmann (2003) parameterization], effectively forming a low-permeability, polycrystalline olivine crucible; (2) the temperature was then increased to the final run temperature, followed by a pressure increase to the final run pressure. Except for 1 GPa experiments, sintering was conducted at pressures 0.1–0.35 GPa below the desired run pressure. For experiments at 1 GPa, we hot-pressed the capsule at 1.4 GPa; but in an effort to retain the relative sense of piston motion (i.e., hot-piston in), we slowly lowered the pressure from 1.4 GPa to below 1.0 GPa before the final temperature ramp, such that when the temperature was increased to its final value the pressure would remain slightly below the desired value; finally, pressure was increased to the final value for the run. Note that in the first of two experiments where we employed this method (Run 51), the pressure was not lowered enough before the final temperature ramp; upon reaching the final run temperature, the pressure was too high and had to be lowered to its target value (hot-piston out). One-atmosphere experiments were conducted using methods similar to Wang and Gaetani (2008): mixtures of MORB glass and powdered Kilbourne Hole olivine were placed in a crucible fabricated from a single crystal of San Carlos olivine and suspended in a flowing mixture of CO_2 and H_2 that produced an fO_2 ~1.7 log units below the QFM buffer, an fO_2 similar to those measured in high-pressure graphite-capsule experiments (Médard et al. 2008); fO_2s for all one-atmosphere experiments are listed in Table 1. The temperatures and pressures shown in Fig. 1a were selected so that the resulting liquids would have approximately 12, 15, and 21 wt. % MgO (hereafter referred to as the ~12, ~15 and ~21 MgO^{liq} series). We were not entirely successful in meeting these target liquid compositions; all of our MgO^{liq} series show decreasing MgO^{liq} with increasing temperature (Fig. 1b). We conducted mostly forward experiments (downward pointing triangles in Fig. 1b) in which low-Ni glass (<0.03 wt. % NiO) was equilibrated with Ni-bearing olivine (~0.37 wt. % NiO). The four reversal experiments (upward pointing triangles in Fig. 1b; run numbers appended with an R in Table 1) used starting glasses doped with 1 wt. % NiO (i.e., higher than in the olivine).

Measurements of all phase compositions are reported in Table 2. Glass and olivine compositions were measured on Caltech's JEOL JXA-8200 using analytical and data processing procedures described by Matzen et al. (2013). Pyroxenes were analyzed on Oxford's JEOL 8600, using an accelerating voltage of 15 keV, a 40 nA beam current, and a 1 μm beam at locations ~10 μm from the edge of each pyroxene grain, utilizing a set of metal (Ni), oxide (Cr_2O_3), and mineral (wollastonite, rutile, jadeite, hematite, rhodonite, periclase, orthoclase) standards. On-peak counts were collected for 30–60 s with high and low backgrounds counted for half of the on-peak time. Pyroxene data acquired at Oxford were processed using the PAP matrix correction (Pouchou and Pichoir 1988). Pyroxenes from some of the runs were also analyzed at Caltech (processed using a modified ZAF correction: CITZAF, Armstrong 1988); for the Caltech data, most of the average pyroxene compositions overlap at one sigma with those obtained from the Oxford analyses and, in all cases, they overlap at two-sigma.

In a reversal experiment, the NiO content of the starting glass is higher than that of a silicate melt in equilibrium with the surrounding olivine. The mass of olivine is large compared to the mass of liquid and NiO diffuses from the liquid into the surrounding olivine over the course of the experiment (generating reverse zoning trends). Olivines that crystallize from the Ni-rich melt at the start of an experiment will have high NiO contents, but the Ni content at their rims decreases with time as the melt continues to lose Ni to the surrounding olivine. Our experiments were never run long enough to fully homogenize all phases, so olivines in contact with a melt pool are strongly zoned near their rims. In an effort to capture the equilibrium partition coefficient, we performed a series of analyses with 1–2 μm step sizes approaching the olivine-glass interface, and interpreted the equilibrium NiO^{ol} to be the last point that showed no contamination from the glass (e.g., Matzen et al. 2013). No such procedure was conducted for the pyroxenes; reported NiO concentrations in pyroxenes from reversal experiments are most likely overestimates of the equilibrium values and they should not be used in the calculation of equilibrium partition coefficients.

Experimental Results

Phase compositions

Glass

Matzen et al. (2013) produced a set of experiments with ~18 wt. % MgO^{liq}. In this work, we produced three additional series of experiments, each with a roughly constant liquid composition but offset from the next series by ~3–4 wt. % MgO. Experiments were conducted at 1-atm and 1–3 GPa and spaced at 25–50°C intervals (see Table 1 and Fig. 1a). All of our experiments produced glasses with MgO contents within 1.2 wt. % of their specified target value, but there are within-series variations. For example, in the ~12 wt. % MgO^{liq} series, the 1-atm experiment produced a glass with 13.2 wt. % MgO because the selected run temperature was too high, whereas other glasses from this series (11.8–12.2 wt. % MgO) are much closer to the target of 12 % (Fig. 1b). Similarly, Run 70 in the ~21 wt. % MgO^{liq} series produced a glass with 21.9 % MgO, higher than the others in the series (20.4–21.3 wt. %). Below, we discuss the extent to which these deviations impact our evaluation of whether or not the temperature dependence of $D_{Ni}^{ol/liq}$ is a significant function of composition. As shown in Fig. 1b, MgO^{liq} decreases in all three experimental series (this study) with increasing temperature. In addition, the ~12, and ~15 MgO^{liq} series (and the ~18 wt. % MgO^{liq} series; Matzen et al. 2013) all exhibit increases in incompatible element concentrations and decreases in SiO_2 contents with increasing pressure

(Table 2). Some variation in melt chemistry within an MgO^{liq} series reflects deviations in the run conditions from those needed to produce the desired melt composition in a run saturated with olivine. As discussed in Matzen et al. (2013), however, we infer that changes in silica largely reflect the crystallization of progressively larger amounts of pyroxene, which has higher SiO_2 contents than the pyroxene-free glasses; (51–56 vs. 47–50 wt. %), as the pressure of the experiments increases (see Table 2 and Fig. 1b). Pyroxene crystallization is also likely at the root of increasing concentrations of incompatible elements in the melt with increasing pressure and temperature (see Matzen et al. 2013). As MgO in the liquid is lowered, pyroxene saturation occurs at progressively lower temperatures and pressures. For example, the 2.0 GPa run (1400°C) in the ~12 wt. % MgO^{liq} series crystallized 31.5 wt. % low- and high-Ca pyroxene, whereas the 3.0 GPa run (1600°C) in the ~21 wt. % MgO series had only olivine and melt.

In general, it was difficult to quench high-MgO liquids to a homogeneous glass in our piston cylinder apparatus, despite using the pressure-drop quench technique of Putirka et al. (1996). Run 59 (Table 2; ~21 wt. % MgO^{liq} series; 2.5 GPa, 1575°C) underwent substantial quench crystallization. We analyzed the quench mats using a 20-μm beam but were unable to reconstruct the melt composition without large errors (Fig. 1b). Even larger errors for quench mats in experiments at ~25 wt. % MgO^{liq} led us to reject them. In addition, experiments at 1.0 and 1.5 GPa experiments in the ~21 wt.% MgO^{liq} series yielded small melt pools that hindered the formation of a homogeneous glass, so no results are reported for these conditions.

Olivine

One feature of our experimental design is that the mass of an experimental charge is dominated by the starting olivine (Table 1); as a result, Mg#s of the olivine in our experiments are expected to vary little from that of the starting olivine (~90; see Table 1 in Matzen et al. 2013). If, however, the melt interacts with a relatively smaller volume of olivine directly adjacent to the melt (e.g., in the 1-atm experiments), the Mg#s of the near-melt olivine are more strongly influenced by the melt composition; for example, at 1-atm, the ~12 and ~15 wt. % MgO^{liq} series melts are in equilibrium with olivines with slightly lower Mg#s (87.5 and 88.7, respectively). In all series, the Al_2O_3 contents of near-melt olivines increase with increasing temperature and pressure; for example, in the ~21 wt. % MgO^{liq} series, Al_2O_3 contents increase from 0.04 at one atmosphere and 1450°C to 0.14 at 3.0 GPa and 1600°C. Olivine-liquid Al partition coefficients measured in our experiments agree well with the predictions of Agee and Walker (1990).

Pyroxene

Low-calcium pyroxene (1.8–2.5 wt. % CaO) is observed in the ~12 and ~15 wt. % MgO^{liq} series experiments, appearing at and above 1.0 and 1.5 GPa, respectively (see Table 1 and Fig. 1b). Subcalcic pyroxenes (6.2–10.4 wt. % CaO) are also present in the ~12 wt. % MgO^{liq} series above 1.0 GPa and in the ~15 wt. % MgO^{liq} series above 2.0 GPa. Na_2O contents of low-Ca pyroxenes increase from 0.1 to 0.3 wt. % with increasing temperature and pressure. The Al_2O_3 contents of both low- and high-Ca pyroxenes also increase with increasing temperature and pressure, from 2 to 8 wt. % in the ~12 wt. % MgO^{liq} series and from 3 to 7 wt. % in the ~15 wt. % MgO^{liq} series. These changes in the Na_2O and Al_2O_3 contents in the pyroxenes are consistent with previous experimental measurements of the pressure and temperature dependence of Na_2O and Al_2O_3 partitioning between pyroxene and silicate melt (e.g., Blundy et al. 1995, Frei et al. 2009). As mentioned briefly above, the SiO_2 contents of the pyroxenes (51–56 wt. %) are higher than those of liquids from pyroxene-free experiments in each series (47–50 wt. % SiO_2). Thus, the crystallization of pyroxene acts to reduce the SiO_2 content of the glass.

Mass Balance

As described in Matzen et al. (2013), phase proportions in our experiments were determined using the non-linear approach of Albarède and Provost (1977) and account for the variable amount of interaction between melt and the enclosing olivine; results are given in Table 1. All mass balance solutions are acceptable at the 95% confidence level (e.g., Press et al. 1992), suggesting that variations in liquid composition are well explained by the observed phases and their compositions (Table 2).

Table 1 includes the calculated change in bulk NiO for the forward experiments. For our piston-cylinder experiments, NiO was conserved in the central melt pool—changes range from –4.2 to +2.1% relative (negative number indicates a decrease). Losses of NiO in 1-atm experiments were larger (–4.7 to –11.5%). We did not mass balance NiO in the reversal experiments as olivines in contact with melt are strongly zoned with respect to Ni.

Attainment of Equilibrium

To demonstrate a close approach to equilibrium, we conducted forward and reversal experiments. As in Matzen et al. (2013), a forward experiment is conducted with a low-NiO glass (<0.03 wt. % NiO) embedded in olivine (0.37 wt. % NiO). Thus, at the beginning of the experiment, the apparent $D_{Ni}^{ol/liq}$ is high, and over the course of the experiment, Ni moves from the olivine into the liquid (measured glasses from these experiments have 0.05 to 0.15 wt. % NiO) and, thus, the apparent $D_{Ni}^{ol/liq}$ *decreases* towards the equilibrium value (and, thus, these forward experiments are indicated by downward pointing triangles in Figs. 1 and 2). The reversal experiments were conducted using a glass doped with ~1 wt. % NiO, similarly surrounded by powdered olivine with 0.37 wt. % NiO. In these experiments, the initial apparent $D_{Ni}^{ol/liq}$ is low, and over the course of the experiment NiO moves from the melt into the olivine so that the apparent $D_{Ni}^{ol/liq}$ *increases* (reversals are shown as upward pointing triangles in Figs. 1 and 2). Where forward and reversal experiments were conducted at the same nominal temperature and pressure, the measured $D_{Ni}^{ol/liq}$ values overlap at one sigma, suggesting that the olivine-liquid Ni partition coefficients reported here closely approach equilibrium values (Fig. 2).

As stated in the Introduction, a goal of this work is to evaluate whether or not the temperature dependence of $D_{Ni}^{ol/liq}$ along the join MORB-Fo_{90} olivine is a significant function of composition. Such a dependency would be manifested in a different slope for $D_{Ni}^{ol/liq}$ vs. temperature for each of the constant composition series. Figure 2 shows $D_{Ni}^{ol/liq}$ values of the ~12, ~15, and ~21 wt. % MgO series experiments from this study (Tables 1 and 2) along with weighted regression lines for each of these series and the ~18 wt. % MgO series of Matzen et al. (2013). The reason for not including the lowest temperature run (open triangle) in the ~12 wt. % series regression is discussed in detail in the Supplemental Information.

Qualitatively, Fig. 2 reinforces the well-known observation that, as MgO^{liq} increases, $D_{Ni}^{ol/liq}$ decreases (e.g., Hart and Davis 1978; Kinzler et al. 1990). However, the salient feature of Fig. 2 for present purposes is that the slopes of all four lines (~12, ~15, ~18, and ~21 wt. % MgO^{liq}) are statistically identical at 2 standard errors (SE): –0.70±1.63/100°C, –0.76±0.21/100°C, –0.63±0.10/100°C, and –0.37±0.14/100°C, respectively (listed uncertainties are 1 SE). The much larger uncertainty associated with the ~12 wt. % MgO^{liq} series reflects the relatively larger errors in $D_{Ni}^{ol/liq}$ and the limited range in temperature. The statistical overlap among the four slopes suggests that, for bulk compositions along the join MORB-Fo_{90} olivine, the temperature dependence of $D_{Ni}^{ol/liq}$ is consistent with being independent of composition, although the progressive decrease in slope in going from liquids with ~15 wt. % MgO to ~21 wt.

% MgO could reflect a small compositional dependence that would be broadly consistent with the calculations of Hirschmann and Ghiorso (1994) on the activity coefficient of $NiSi_{0.5}O_2$ in silicate liquids. Keeping in mind that increasing temperature can be associated with increasing pressure, the results shown in Fig. 2 also confirm the conclusion of Matzen et al. (2013) that, for constant liquid and olivine compositions, $D_{Ni}^{ol/liq}$ decreases with increasing temperature and pressure. In the following section, we fit our partitioning data using a thermodynamically-inspired model that accounts for temperature and compositional effects on $D_{Ni}^{ol/liq}$ and we show that all but one of the 28 experiments that comprise the four MgO series are consistent with a single regression line in 1/*T*(K) space.

Discussion

Modeling $D_{Ni}^{ol/liq}$: ideal exchange reaction

Following Matzen et al. (2013) and many others (e.g., Hart and Davis 1978; Leeman and Lindstrom 1978; Kinzler et al. 1990), we fit our data using a Ni-Mg exchange reaction:

$$MgSi_{0.5}O_2^{ol} + NiO^{liq} \leftrightarrow NiSi_{0.5}O_2^{ol} + MgO^{liq}, \tag{1}$$

for which we write the following expression:

$$\Delta_{r(1)}G^{\circ}_{T,P} = -RT\ln\left(\frac{X^{ol}_{NiSi_{0.5}O_2}X^{liq}_{MgO}}{X^{ol}_{MgSi_{0.5}O_2}X^{liq}_{NiO}} \times \frac{\gamma^{ol}_{NiSi_{0.5}O_2}\gamma^{liq}_{MgO}}{\gamma^{ol}_{MgSi_{0.5}O_2}\gamma^{liq}_{NiO}}\right), \tag{2}$$

where $\Delta_{r(1)}G^{\circ}_{T,P}$, the standard-state Gibbs free energy change of reaction (1) at temperature (*T*, in Kelvin) and pressure (*P*, in bars), is independent of composition. X_i^{φ} and γ_i^{φ} are the mole fraction and activity coefficient of the i^{th} component in phase φ, using the molar components of Matzen et al. (2013), and *R* is the gas constant. One of the benefits of an exchange reaction is that, over moderate ranges in temperature and pressure, $\Delta_{r(1)}C_p^\circ$ and $\Delta_{r(1)}V$ are small enough to be safely neglected in the computation of $\Delta_{r(1)}G_{T,P}^\circ$, so that the standard-state changes in enthalpy and entropy for reaction (1) can be approximated as constants and the effect of pressure on $D_{Ni}^{ol/liq}$ is small [see Matzen et al. (2013) for a more detailed exposition of this important point]. Furthermore, at high temperatures, olivine can be treated as an ideal solution (e.g., Nafziger and Muan 1967; Campbell and Roeder 1968) and, as discussed by O'Neill and Eggins (2002) and O'Neill and Berry (2006) among others, the ratios of activity coefficients for divalent cations in silicate liquids can be approximated as a constant. Using these assumptions and defining a molar partition coefficient, $D_{Ni}^{molar} = \frac{X_{NiSi_{0.5}O_2}^{ol}}{X_{NiO}^{liq}}$, equation (2) simplifies to

$$-\frac{\Delta_{r(1)}H_{T_{ref},P_{ref}}^\circ}{RT} + \frac{\Delta_{r(1)}S_{T_{ref},P_{ref}}^\circ}{R} = \ln\left(D_{Ni}^{molar}\right) + \ln\left(\frac{X_{MgO}^{liq}}{X_{MgSi_{0.5}O_2}^{ol}}\right), \tag{3}$$

which was presented as equation (5) in Matzen et al. (2013). They fit their data and data from the literature to equation (3) and showed that the Ni-Mg exchange reaction has a significant temperature dependence. Although not discussed here, exchange reactions between Mg and other divalent cations (e.g., Mn and Fe^{2+}) show little temperature dependence (Roeder and Emslie 1970; Matzen et al. 2011, 2013), making Ni unusual in this respect. Since previous work suggested a strong effect of liquid composition on activity coefficients of the $NiSi_{0.5}O_2$ component in silicate melts (Hirschmann and Ghiorso 1994), we seek to determine the extent to which compositional contributions to the temperature-dependence of the Ni-Mg exchange reaction can be ignored (i.e., that the ratio of MgO^{liq} and NiO^{liq} activity coefficients is approximately constant).

Figure 3 shows $\ln\left(K_{D,Ni-Mg}^{ol/liq}\right) = \ln\left(D_{Ni}^{molar}\right) + \ln\left(\frac{X_{MgO}^{liq}}{X_{MgSi_{0.5}O_2}^{ol}}\right)$ plotted against inverse temperature for experiments from this work and Matzen et al. (2013). The solid blue line in Fig. 3 is a weighted least-squares fit to all of the data (dashed curves represent the 95% confidence bounds). The data clearly define a non-zero slope, which can be equated to $-\frac{\Delta_{r(1)}H^{\circ}_{T_{ref},P_{ref}}}{R}$ via equation (3) so that the Ni-Mg olivine exchange reaction is temperature dependent. Significantly, all of the data, with one exception (see Fig. 3), overlap the best-fit line at 2σ (75% of the 28 points overlap at 1σ), indicating that the experimental data (with MgO^{liq} contents that vary by nearly a factor of two) are consistent with single values of $-\Delta_{r(1)}H^{\circ}_{T_{ref},P_{ref}}/R$ and $\Delta_{r(1)}S^{\circ}_{T_{ref},P_{ref}}/R$. Further, all constant-composition series exhibit statistically equivalent temperature dependencies (i.e., slopes for the ~12, ~15, and ~21 wt. % MgO^{liq} series (this study) and the ~18 wt. % MgO series (Matzen et al. 2013), all overlap at 1 SE: 2,161 ± 2,598; 5,000 ± 1,075; 3,943 ± 712, and 4,248 ± 1,166 (K), respectively). In our discussion of Fig. 2, we separated out the lowest temperature experiment in the ~12 MgO^{liq} series but this is included in Fig. 3 because differences in MgO content of the melt are accounted for by the term that includes X_{MgO}^{liq} in equation (3). Note also that the slope reported here for the ~18 wt. % MgO^{liq} experiments of Matzen et al. (2013), 3,943 ± 712, differs from that reported by Matzen et al. (2013), 4,375 ± 1,050. Here, fits are weighted by errors on $K_{D,Ni-Mg}^{ol/liq}$ whereas Matzen et al. (2013) used an iterative, bisquare-weighted least-squares fit. When the errors on all data are known, using weights that are proportional to the inverse square of the compositional errors should result in superior estimates of the fit parameters (including uncertainties), compared to a bisquare-weighted fit. As noted above, the blue line in Fig. 3 is a weighted fit to all of our results simultaneously (i.e., to a combination of the new results presented here plus our previously published experiments with ~18 wt. % MgO in the melt); $-\Delta_{r(1)}H^{\circ}_{T_{ref},P_{ref}}\Big/R$ and $\Delta_{r(1)}S^{\circ}_{T_{ref},P_{ref}}\Big/R$ for this best-fit line are 3641 ± 396 (K) and −1.597± 0.229, respectively, and *both* temperature ($-\Delta_{r(1)}H^{\circ}_{T_{ref},P_{ref}}\Big/R$ is nonzero) and the compositions of olivine and liquid affect $D_{Ni}^{ol/liq}$. If the assumptions made in deriving equation (3) are correct, we expect that the standard-state parameters obtained from fitting individual constant-composition series will be identical to each other within uncertainty and, as noted above, this expectation is met.

In Fig. 4, our results are plotted together with a compilation of literature data. The Filter-B data set (from Matzen et al. 2013), which uses analytical totals (98.5–101.5 wt. %) and Ni loss (<65 %) as filtering criteria, has been updated to include data from this study; we refer to this amended data set as Filter-B′. Fitting the exchange reaction to the Filter-B′ data set (using an iterative, bisquare-weighted least-squares technique since not all studies report compositional uncertainties) gives a temperature dependency (4,321 ± 190 K; 183 experiments; red line in Fig. 4) that overlaps within 2 SE of the slope obtained for the high-precision data shown in Fig. 3 (3,641 ± 396 K; 28 experiments; the blue line in Fig. 4).

The Filter-B′ data set displays considerable scatter in Fig. 4. Some of this may be due to analytical errors or disequilibrium, but it is important to emphasize that this data set spans a large compositional range. For example, glass SiO_2, Al_2O_3, FeO* (all Fe as FeO), CaO, and Na_2O contents range from 40.5–68.8, 0–21.5, 0–37.2, 0–29.1, and 0–11.1 wt. %, respectively, and olivine Mg#s range from 36 to 100. In comparison, glasses from this study and Matzen et al. (2013) are more restricted: SiO_2, Al_2O_3, FeO*, CaO, and Na_2O contents range from 44.4–50.2, 9.1–14.8, 9.3–12.4, 6.3–10.4, and 1.4–3.5 wt. %, respectively, and olivine Mg#s ranging from 86 to 91. Given the broad range in bulk and phase compositions, it is possible, indeed likely, that the simplifications we made in arriving at equation (3)—especially that the ratio of activity coefficients for MgO^{liq} and NiO^{liq} is constant—do not hold for all of the literature experiments. Ghiorso and Sack (1995) commented on this issue when they stated that "…workers who have focused their effects on thermodynamic modeling of simple melt systems (see Berman and Brown 1987, for a synthesis and review) have demonstrated that quite complicated models are required to achieve the same level of data reproducibility as simpler formulations… provide in magmatic [natural] liquids." Unfortunately, quantifying the extent to which the ratio of MgO^{liq} and NiO^{liq} activity coefficients varies for all the experimental liquids in the Filter-B′ data set is difficult. Although there has been substantial work on determining how NiO^{liq} activity coefficients vary with temperature and liquid composition, most of the experiments have been conducted using the 1-atm diopside-anorthite eutectic as a base composition, and thus it is unclear whether a global fit to that data (e.g., Wood and Wade 2013) is applicable to the much wider range of liquid compositions encompassed by the Filter-B′ compilation. A similar situation exists for estimating MgO^{liq} activity coefficients; the activity model of Snyder and Carmichael (1992) is calibrated on natural silicate melts, and the activity models of Berman (1983) are tied to compositions in the system CaO-MgO-Al_2O_3-SiO_2 (CMAS). Motivated by Ghiorso and Sack (1995), we note that many of the outliers in Fig. 4 are experiments from systems where Al_2O_3 or CaO are either absent or present at very low concentrations, < 2 wt. %, in the liquid (open symbols in Fig. 4). Therefore, we also show a refit to the Filter-B′ data set (black line; Fig. 4) after removing those 53 experiments where the bulk composition did not contain at least CMAS+NiO and the liquid ≥ 2 wt. % each of Al_2O_3 and CaO (labeled Complex Filter-B′ on Fig. 4). Note that the scatter is reduced (the mean percent error on $D_{Ni}^{ol/liq}$ for the Complex Filter-B′ data set is 9.6% compared to 11.3% for Filter-B′), but the slope of the line (4,505 ± 196; 130

experiments) overlaps at 1 SE with that based on the entire Filter-B′ data set (4,321 ± 190) and at 2SE for the fit obtained from the experiments in this study combined with those of Matzen et al. (2013), 3,641 ± 396. Since our goal is to generate a simple predictive tool to model $D_{Ni}^{ol/liq}$ in natural olivine-bearing liquids as a function of temperature and melt composition, we prefer the Complex Filter-B′ fit in Fig. 4. In the Supplemental Information, we provide a more detailed discussion of the quality of the fit of equation (3) to the experimental data as well as a comparison with the temperature-independent $D_{Ni}^{ol/liq}$ model of Beattie et al. (1991). Finally, although Matzen et al. (2013) concluded that ΔV for the exchange reaction (equation 1) was small enough to ignore, we briefly revisited this issue by explicitly including a ΔV term in our fit to the Complex Filter-B′ data set (ΔC_p° was assumed to be zero). Consistent with the conclusions of Matzen et al. (2013), ΔV is small, –0.024 ± 0.015 J/mol, and the improvement in the fit is not statistically significant at the 95% confidence level.

Rearranging equation (3) and substituting in our preferred values of $-\Delta_{r(1)} H^{\circ}_{T_{ref},P_{ref}} \big/ R$ and $\Delta_{r(1)} S^{\circ}_{T_{ref},P_{ref}} \big/ R$ yields an expression:

$$D_{Ni}^{molar} = \exp\left[\frac{4{,}505 \pm 196}{T} - 2.075 \pm 0.120 - \ln\left(\frac{X_{MgO}^{liq}}{X_{MgSi_{0.5}O_2}^{ol}}\right)\right] \quad (4)$$

that can be used to calculate $D_{Ni}^{ol/liq}$, provided we have estimates of temperature and the MgO contents of the olivine and melt. The composition of the melt and the Mg# of olivine are typically known or assumed and, therefore, the corresponding temperature is readily determined using expressions explicit in temperature (e.g., Beattie 1993; Putirka et al. 2007) or any of a number of petrological programs, including MELTS (Ghiorso and Sack 1995) and Petrolog3 (Danyushevsky and Plechov 2011).

The influence of lithospheric thickness on the NiO contents of olivine phenocrysts

In this section, we explore the influence that a temperature-dependent $D_{Ni}^{ol/liq}$ has on olivines erupting onto lithosphere of varying thickness. McKenzie and Bickle (1988), Ellam (1992), and Fram and Lesher (1993) provided early discussions of the potential influence of lithospheric thickness on the composition of erupted magmas. More recently, Sobolev et al. (2007) noted that lavas from areas with thick lithosphere (>70 km, e.g., Hawaii) tend to have magnesian olivines with higher NiO concentrations than those erupted onto thin lithosphere (e.g., Iceland), and to have higher concentrations than the values in mantle olivine (e.g., ~0.37; Korenaga and Kelemen 2000; Herzberg et al. 2013). They rationalized these observations as being a consequence of adiabatically rising parcels of mantle consisting of thermally (but not chemically) equilibrated packages of eclogite/pyroxenite and peridotite. As the mantle adiabatically ascends, the more fertile eclogite domains are the first to extensively melt (e.g., Hirschmann and Stolper 1996; Stolper and Asimow 2007; Lambart et al. 2016) and the resulting silica-rich liquids react with the surrounding peridotite to produce zones of olivine-poor to olivine-free, Ni-rich metasomatic pyroxenites. With continued upwelling, both the pyroxenite and the peridotite partially melt (although with different productivities) resulting in primary lavas that are mixtures of liquids originating from these two lithologies. The lithosphere limits the final pressure of partial melting so that melts produced beneath a thick lithosphere are dominated by those from the metasomatic pyroxenite; partial melts of these pyroxenites are Ni-rich both because the pyroxenites are rich in Ni relative to most known mantle-derived pyroxenites (e.g., France et al. 2015) and also because these olivine-poor source rocks have low bulk D_{Ni} values, and thus the olivines that precipitate from these melts are consequently predicted to be anomalously Ni-rich. In contrast, partial melts produced beneath a thin lithosphere are diluted by more extensive contributions of melt from the peridotite, thus diluting the influence of the Ni-rich melts produced by melting of pyroxenite and resulting in olivine phenocrysts from shallow melting that are Ni-poor relative to those from deeper melting. In the Sobolev et al. (2007) model, the composition of the mantle source (i.e., the relative amounts of pyroxenite), the mantle potential temperature, and the thickness of the lithosphere all influence the NiO contents of olivine phenocrysts crystallized from mantle-derived basalts. It is important to stress that this model, in the context of Ni contents of magnesian olivine phenocrysts, is driven by the assumption that $D_{Ni}^{ol/liq}$ is a function only of composition—given such an assumption, it is difficult to generate olivine phenocrysts with Ni contents significantly higher than those of olivine in the mantle source by low degrees of high-pressure partial melting followed by low-pressure crystallization.

Recently, a number of authors (Li and Ripley 2010; Niu et al. 2011; Putirka et al. 2011; Matzen et al. 2013) have suggested an alternative explanation for high-NiO olivine phenocrysts in localities such as Hawaii. These authors proposed that the crystallization of such olivine from basalts at low pressure results from a temperature (and/or pressure) dependent $D_{Ni}^{ol/liq}$. In this class of models, a thick lithosphere imposes a large difference in temperature and pressure between a partial melt equilibrating with the mantle (generally presumed to be peridotitic), and the near-surface environment in which olivines begin to crystallize. Thus, it is the effect that lithospheric thickness has on the temperature and pressure difference between the conditions of melt segregation in the mantle and the cooler near-surface conditions at which forsteritic olivine phenocrysts grow that controls their NiO contents and that larger temperature differences lead to higher NiO contents in early crystallized olivines.

As noted above, Matzen et al. (2013) showed that the effect of pressure on $D_{Ni}^{ol/liq}$ is negligible for depths down to ~100 km (i.e., from 0–3 GPa)—a depth range that encompasses much of the variations in thickness of the oceanic lithosphere (e.g., Artemieva 2011). With our new olivine-melt partitioning data, we can test the hypothesis that a temperature-dependent $D_{Ni}^{ol/liq}$ and partial melting of a peridotitic source control the NiO contents of near-surface olivine phenocrysts. To compute an expected difference between the NiO content of a primary olivine phenocryst and lithospheric thickness, we use

$$\frac{X_{NiSi_{0.5}O_2}^{mole} @ T_{1-bar}}{X_{NiSi_{0.5}O_2}^{mole} @ T_m} = \exp\left[\frac{-\Delta_{r(1)} H^{\circ}_{T_{ref},P_{ref}}}{R}\left(\frac{1}{T_{1-bar}} - \frac{1}{T_m}\right)\right], \tag{5}$$

after equation (8) from Matzen et al. (2013). This equation is derived from two statements of equation (3) for $D_{Ni}^{ol/liq}$ involving two different temperatures: one for a primary olivine-saturated melt in the mantle source at a temperature of T_m, and a second, for the same melt, at its 1 bar olivine-saturated liquidus, $T_{1\text{-}bar}$. Given the temperature at which olivine begins to crystallize at low pressure ($T_{1\text{-}bar}$) and assuming: (1) the Ni content of mantle olivine in the source region; (2) that the mantle melt last equilibrated at the base of the lithosphere; and (3) that the melt composition remained constant between the source and the site of phenocryst growth (and thus that the initial low-pressure olivine has the same Mg# as that in the mantle source, i.e., the olivine-liquid Fe^{2+}-Mg exchange reaction is not a strong function of P and T; Toplis 2005), we can obtain T_m using the slope of the olivine-saturated liquidus (55°C/GPa, Sugawara 2000). Equation (5) can then be used to predict the NiO content of initially crystallizing near-surface olivines as a function of lithospheric thickness. As discussed in Matzen et al. (2013), the slope of the olivine-saturated liquidus estimated by Sugawara (2000) is very similar to values derived from MELTS (Ghiorso and Sack 1995) calculations and from equation (4) of Putirka et al.

(2007); temperatures at 3 GPa obtained by applying the polynomial “pressure-correction” of Herzberg and O’Hara (2002) to the 1-atm olivine-liquid geothermometer of Beattie (1993) are within 15°C of those calculated using Sugawara’s 55°C/GPa.

We assume that mantle olivines in the source region have 0.37 ± 0.03 wt. % NiO (median ± MAD, mean absolute deviation; data for spinel lherzolites from Korenaga and Kelemen 2000; Korenaga personal communication 2011), a value that overlaps with that for olivines from abyssal peridotites, 0.38 ± 0.03 (median ± MAD) (Hamlyn and Bonatti 1980; Shibata and Thompson 1986; Bonatti et al. 1992; Edwards and Malpas 1996; Ghose et al. 1996; Stephens 1997; Hellebrand et al. 2002; Brunelli et al. 2003; Seyler et al. 2003; Rampone et al. 2004; Warren and Shimizu 2010). Note that the spinel lherzolites considered by Herzberg et al. (2013) have an identical median but a smaller uncertainty (MAD = 0.01); in the following discussion, we use the error calculated using the Korenaga and Kelemen (2000) data set, as it is based on nearly twice as many analyses and reflects near global coverage. For a lithospheric thickness of zero, there is no temperature contrast between source and surface, so equation (5) recaptures the NiO content of the mantle olivine (i.e., 0.37 wt. % NiO). With a thicker lithosphere, there is a temperature difference between the source and olivine saturation near the surface and our calculations predict that these low-pressure olivines will have higher NiO than those present in the mantle source region. Although it is the difference between T_m and $T_{1\text{-}bar}$ in equation (5) that leads to differences in the Ni contents of the low-pressure olivines that crystallize from primary melts, it is inverse temperatures that appear in equation (5) and this means that variations in the 1-bar liquidus temperature (reflecting variations in primary melt composition, principally MgO content) have, as we show below, only a small effect on calculated Ni in low-pressure olivines. We used estimates of mantle potential temperature, T_P, at mid-ocean ridge and hot-spot settings

(~1325–1570°C; Iwamori et al., 1995; Kinzler 1997; Ito et al. 1999; Asimow and Langmuir 2003; Courtier et al. 2007; Herzberg and Asimow 2008; Lee et al. 2009; Brown and Lesher 2014; Gale et al. 2014; Shorttle et al. 2014) (but see Putirka et al. 2007 for much higher estimates) and the expression from Herzberg and Asimow (2015) relating T_P to a 1-bar liquidus temperature to acquire an estimate for the range in $T_{1\text{-}bar}$ values, 1266–1447°C (with a mid-point of 1356°C), which most likely covers the vast majority of low-pressure liquidus temperatures for primary basaltic and picritic magmas (e.g., Herzberg et al. 2007).

In Fig. 5, the solid black line was obtained using the above mid-point 1-bar liquidus temperature, 1356°C in equation (5) coupled with the linear relationship in pressure between $T_{1\text{-}bar}$ and the temperature of melt segregation from the mantle (T_m) [the widening gray band shows the effect of using the minimum and maximum $T_{1\text{-bar}}$ values, 1266 and 1447°C, in equation (5)]. The fact that the gray band is quite narrow, even at 110 km (where $T_m – T_{1\text{-}bar}$ = ~192°C) shows that a difference of 181°C at 1 bar (1266 to 1447°C), does not have a large effect on the calculated 1-bar olivine NiO content, even if the primary magma separates from its source at ~3.5 GPa (110 km). In contrast, variations in mantle olivine Ni content can have a large effect—the dashed lines reflect the uncertainty in the NiO content of the peridotite source (± 0.06; 2×MAD calculated using the mid-point temperature (1356°C). The error in $\frac{-\Delta_r H^\circ_{T_{ref},P_{ref}}}{R}$ can be ignored for present purposes (e.g., at a lithospheric thickness of 90 km, the propagated error on the calculated NiO from the uncertainty in $\frac{-\Delta_r H^\circ_{T_{ref},P_{ref}}}{R}$ is only ±0.005 wt. %). The average calculated increase in the expected low-pressure olivine NiO content due to lithospheric thickness controlling the depth at which the primary magma separates from its mantle source coupled with the temperature dependence of $D_{Ni}^{ol/liq}$ is ~0.114 wt. % per 100 km.

In Fig. 5, we compare our model 1-bar olivine NiO contents calculated as a function of the depth of primary melt segregation to observed nickel contents in olivine phenocrysts from MORBs and lavas from the Hawaiian-Emperor Seamount chain (H-E), the Galápagos, the North Atlantic Igneous Provence (NAIP; Iceland, West Greenland, and Baffin Island/Bay), Réunion, the Azores, and the Canary Islands (see caption for island abbreviation) plotted as a function of depth to the lithosphere-asthenosphere boundary (LAB) at the time of eruption (drawn largely from Dasgupta et al. 2010; other data sources are noted in Table S1). Olivine analyses for the Galápagos are from Vidito et al. (2013); for West Greenland and Baffin Island/Bay, data from Herzberg et al. (2016) were combined with those of Sobolev et al. (2007); analyses for the other localities are from Sobolev et al. (2007). Our model NiO olivine contents are calculated assuming no olivine crystallization as the primary magma migrates from its source region to the surface. It is, therefore, important to compare these calculated NiO values to those in the most primitive olivine phenocrysts at each of the localities as these primitive olivines are presumably closest in Ni composition to those that crystallized from the "primary" magmas. For each of the locality/suite of lavas, a plot of olivine Mg# vs. olivine NiO defines either a relatively linear or curved trend. In order to estimate the "average" NiO content in the most primitive (i.e., highest Mg#) olivine in each of the suites of lavas, we fit each suite of data to either a linear or power law expression by minimizing the sum of the absolute deviations (in four of the 44 suites, samples defined two coherent trends and both were fit and in six of the 44, a subset of the samples defined a much more coherent trend in $\mathrm{Mg\#}^{ol}$ vs. NiO^{ol} space compared to the entire suite and, in these cases, only the subset was used; see notes to Table S1). The olivine with the highest Mg# in a given suite (or subset) was then used to calculate a NiO content ($\mathrm{NiO}_{\text{max-Mg\#}}$) based on the regression equation for that suite—in this way, the plotted NiO content for each locality/suite of lavas (Fig. 5) reflects all or a large portion of the olivines analyzed for that suite (further details concerning the sample suites, e.g., the designations “tholeiitic”, “alkalic”, and “uncertain” in Fig. 5, are discussed in the notes to Table S1; regression coefficients are reported in Table S2).

Figure 5 shows that the $\mathrm{NiO}_{\mathrm{max\text{-}Mg\#}}$ values of olivine phenocrysts from MORBs and various OIBs are positively correlated with lithospheric thickness, consistent with the observation of Sobolev et al. (2007) and, although the scatter of the data points is large, suggesting that other factors are also at work, the positive correlation between lithospheric thickness and $\mathrm{NiO}_{\mathrm{max\text{-}Mg\#}}$ for the data plotted in Fig. 5 is significant at greater than the 99% confidence interval (Spearman rank-order correlation coefficient = 0.709). A weighted least-squares fit of olivine $\mathrm{NiO}_{\mathrm{max\text{-}Mg\#}}$ vs. depth to the LAB, using only those nickel contents from localities with maximum olivine Mg#s of ≥ 89 yields a slope per 100 km of 0.105 ± 0.006 wt. % NiO. Note that the observed change in maximum NiO with increasing depth is consistent with the slope from the model $T_{1\text{-}bar} = 1356°\mathrm{C}$ curve in Fig. 5 (0.114 wt. % NiO/100 km) and, thus, the overall trend of increasing NiO in the most magnesian olivine phenocrysts in lavas erupted above lithosphere of increasing thickness is consistent with a temperature-dependent $D_{Ni}^{ol/liq}$ and a mantle source region (dominantly peridotite) with olivines that contain ~0.37 ± 0.06 wt. % NiO. It is perhaps significant that both tholeiitic and alkalic basalts show a positive correlation in Fig. 5 suggesting that the same overall mechanism controls the Ni contents in both of these compositionally distinct groups of lavas. We want to emphasize that we are not asserting that source regions of the lavas shown in Fig. 5 are exclusively peridotitic in composition. The presence of pyroxene-rich lithologies has been widely invoked to account for aspects of the geochemical and isotopic variability in oceanic basalts (e.g., Hirschmann and Stolper 1996;

Harpp and White 2001; Hofmann 2003; Huang and Frey 2005; Jackson et al. 2012; Lambart et al. 2013; Brown and Lesher 2014; Shorttle et al. 2014) and the presence of pyroxene-rich lithologies in the source regions may well contribute to some of the observed scatter in Fig. 5 (e.g., in samples from the Hawaiian-Emperor chain). Nevertheless, the positive correlation between $\text{NiO}_{\text{max-Mg\#}}$ and lithospheric thickness suggests an important role for a temperature dependent $D_{Ni}^{ol/liq}$, as does the positive correlation between olivine NiO contents and olivine-spinel temperatures calculated for MORBs and basalts from large igneous provinces (Coogan et al. 2014). Finally, Herzberg et al. (2016) suggested that the nickel contents of olivines in West Greenland and Baffin Island Paleocene picrites are inconsistent with a temperature-dependent $D_{Ni}^{ol/liq}$ given the estimated depths of melt segregation of these lavas. However, Fig. 5 shows that both the West Greenland and the Baffin Island/Bay data are, in fact, consistent with the model curve based on equation (5). (See Supplemental Information for a brief discussion of the apparent contrasting conclusions of Dasgupta et al. (2010) on the depth of melt equilibration for OIBs).

Even though the correlation between olivine $\text{NiO}_{\text{max-Mg\#}}$ and depth to the LAB is statistically significant, several of the MORB, Icelandic, and Galápagos suites plot below the dashed lower bound (–2×MAD on the median mantle olivine NiO content). Furthermore, the y-intercept of the weighted fit to $\text{NiO}_{\text{max-Mg\#} \geq 89}$ vs. lithospheric thickness discussed above is 0.33 wt. %, below the accepted median NiO content in peridotitic olivines (0.37 wt. %), although still within two mean absolute deviations of the median value. Two possible explanations for these deviations are: (1) partial re-equilibration of the parental melts with the lithosphere as the liquids migrate to the surface and/or lithosphere erosion (both processes would move points to lower LAB depths in Fig. 5), and (2), not sampling the most primitive and thus highest Ni olivine in a suite of samples. Interactions between ascending parental melts and the lithosphere are likely. However, for Hawaii, both low- and high-silica magmas are observed (Rhodes and Vollinger 2004; Stolper et al. 2004) and compositions of melt inclusions in Hawaiian olivines are highly variable (e.g., Sobolev et al. 2000), suggesting that interactions of mantle melts with the lithosphere were insufficient to destroy their geochemical characteristics. In the remainder of this section we focus on the second possible explanation, that of the vagaries of sampling.

Given that Ni is strongly partitioned into olivine and that olivine is generally the only silicate phase on the liquidus of primitive basalts at low pressures, the scatter to low Ni values in Fig. 5 may reflect the vagaries of sampling—i.e., the most Fo-rich olivines that crystallized from the parental magmas associated with a given suite were not analyzed (most of the low NiO data points in Fig. 5 are denoted by open symbols indicating that the maximum olivine Mg# for these suites is < 90). There are at least two possible explanations for these anomalously low $NiO_{max-Mg\#}$ values that could reflect incomplete sampling:

- The first possibility is that the most primitive olivines are present in the lavas, although in low abundance, but are easily overlooked. This can be understood using the HSDP2 Mauna Kea data set of Sobolev et al. (2007), which contains 3869 olivine analyses from 42 polished thin sections. In 41 of these sections, there is no olivine analysis with an Mg# within 0.5 of the maximum value of 90.99 found in section SR277-8.0, and only 74 analyses (2 %) have Mg#s within 1 unit of the maximum observed value (these 74 olivines are distributed among 11 thin sections). A simple Monte Carlo calculation indicates that, had only three thin sections out of the 42 been analyzed (three being the median number of samples per suite/distinct population; see Table S1), then the likelihood of “capturing” the 90.99 value falls to ~7% and the probability of analyzing an olivine with an Mg# ≥ 90 is

~57% (assuming that all olivine phenocrysts are analyzed in each thin section). Note that the range of olivine compositions for many of the suites plotted in Fig. 5 are based on a small number of samples and a small number of analyses (i.e., not all available olivines in the chosen sections were analyzed). Thus, for those suites where the maximum observed Mg$\#^{ol}$ is less than ~90 and where a relatively small number of olivines were analyzed, it is plausible that the most primitive olivines present were missed.

- The second possibility is that the most primitive olivines were never erupted. Large piles of cumulate olivine are thought to lie beneath Hawaiian volcanoes (e.g., Clague and Denlinger 1994), and seismic refraction studies suggest that large volumes of gabbro exist beneath ocean islands that sit on thinner lithosphere (e.g., Galápagos; Richards et al. 2013). Furthermore, petrologic and geochemical arguments have been used to argue that high-pressure fractionation is an important process for MORBs from Knipovich Ridge (labeled "K" in Fig. 5, Hellevang and Pedersen 2005), in Iceland (e.g., Maclennan 2008; Winpenny and Maclennan 2011), and in the Galápagos (e.g., Geist et al. 1998). Therefore, magma chambers may act as density filters that prevent the earliest fractionation products (i.e., high-NiO olivines) from being erupted. Alternatively, based on extensive data from Icelandic lava flows, Thomson and Maclennan (2013) suggest that the majority of olivine phenocrysts are not in chemical equilibrium with their surrounding magma, and that the olivine phenocrysts have resided in cumulate mush piles at the base of crustal magma chambers, where high NiO concentrations in olivine are likely to have been muted by diffusive re-equilibration [note that deformed olivine phenocrysts in picritic Hawaiian lavas have also been used to argue that they are not directly related to their entraining magma (e.g., Garcia 1996; Baker et al. 1996; Sakyi et al. 2012)]. Thus, magma chambers may act as density filters preventing primitive olivines from erupting, and/or (given sufficient residence times) serving to homogenize olivine compositions through diffusive re-equilibration.

Since olivine residence times and entrainment processes are stochastic, most basaltic suites may contain olivines whose Ni contents either reflect or approach those values expected of olivines in equilibrium with the primary (or parental) magmas that have entered the system (e.g., Fig. 5)—although, as discussed above, the number of analyses required to discover olivines with these primitive Ni values may number in the hundreds to thousands. It is our hope that by using data sets with large numbers of analyses, and focusing on the NiO contents of the most Mg-rich olivine observed, we can minimize the effect of sampling “biases” of the sort described above.

Finally, a potential test of the extent to which the various sampling and petrologic issues discussed above were operative is to plot $NiO_{max\text{-}Mg\#}$ values vs. the maximum observed olivine Mg# for a given suite. Figure 6 shows that for MORBs and tholeiites from Iceland and Hawaii—those petrologic provinces where we have the most tholeiitic suites, the maximum olivine NiO and Mg# are positively correlated. If the most magnesian olivines in these low NiO^{ol} suites have not been sampled, the trends in Fig. 6 suggest that the low $NiO_{max\text{-}Mg\#}$ MORB, Icelandic, and Hawaiian suites might, thereby, project to higher NiO^{ol} values and become more consistent with the model curve of Fig. 5.

Given the factors discussed above that can skew compositions of entrained olivines in erupted lavas to lower Mg#s and nickel contents, the general agreement between the NiO contents of primitive olivine phenocrysts and the model curve shown on Fig. 5 is encouraging and consistent with lithospheric thickness controlling the depth at which melts last equilibrate with a largely peridotitic mantle.

Conclusions

We performed experiments over a range of temperatures (1300–1600°C) and pressures (1-atm–3.0 GPa) to separate the effects of temperature from those of liquid composition on the partitioning of Ni between olivine and silicate melt. The results of these experiments are subsets of glasses with approximately constant compositions (~12, ~15, and ~21 wt. % MgO) co-existing with olivine. We parameterized our partitioning data using a Ni-Mg exchange reaction and, at 2 SE, the resulting temperature dependencies overlap with each other, with the temperature dependency of the ~18 wt. % MgO^{liq} series determined by Matzen et al. (2013), and with a global set of data that spans a wide range of olivine and liquid compositions (this study, Matzen et al. 2013, and experiments from the literature). The relative insensitivity of $D_{Ni}^{ol/liq}$ obtained in this work to liquid composition makes the predictive model applicable to a wide range of natural melts.

The temperature dependence of $D_{Ni}^{ol/liq}$ causes the NiO contents of primitive near-surface olivine phenocrysts to scale with the temperature contrast between mantle melting and low-pressure crystallization and, if primary melts last equilibrate with the mantle near the lithosphere-asthenosphere boundary, then a correlation between NiO contents of initially crystallizing olivine and lithospheric thickness is a natural consequence of this temperature dependence of $D_{Ni}^{ol/liq}$. Our predictions compare favorably with the observed increase in NiO contents of high-Mg# olivine phenocrysts with lithospheric thickness, suggesting that these variations in observed NiO contents may reflect melting of and equilibration with mantle peridotite under lithospheric lids of varying thickness.

Acknowledgments

We thank Aaron Wolf for statistical guidance and Ma Chi for assistance with the electron microprobe. Funding was provided by National Science Foundation grant EAR-1019886, National Aeronautics and Space Administration grant NNG04GG14G, and European Research Council grant 267764

Figure 1.

Experimental run conditions and melt compositions for experiments in this work and Matzen et al. (2013). (a) Pressure as a function of temperature. Filled circles and associated dashed lines correspond to series with similar glass compositions. (b) Symbols denote concentration of MgO (wt. %) in glass as a function of temperature; multiple symbols at a given temperature for a specific MgO-series reflect forward and reverse experiments at those *P*-*T* conditions (for this study, downward and upward pointing triangles, respectively); dashed lines associated with each MgO-series are weighted least-squares fits. Low-Ca (L) and high-Ca (H) pyroxenes are indicated, where present in the run products. Error bars in this and succeeding figures are one standard deviation of the mean, unless otherwise stated, and are shown where larger than the size of the symbol. The large error bars on the 1575°C experiment (~21 wt. % MgO series) are a consequence of quench crystallization.

Figure 2.

$D_{Ni}^{ol/liq}$ (by weight) vs. temperature for the new experiments presented here and those of Matzen et al. (2013), which are represented by the solid black line (a weighted least-squares fit).

Downward and upward pointing triangles represent forward and reversal experiments, respectively; error bars are propagated from the analytical uncertainties reported in Table 2. The open symbol is for a run (# 68) deemed to have too magnesian a liquid composition to be included with the ~12 wt. % MgO series experiments (see Supplemental Information for further discussion). Dashed lines are weighted least-squares fits to each respective series from this study. As discussed in the text, the slopes of all four lines are the same within uncertainty.

Figure 3.

$\ln\left(K_{D,Ni-Mg}^{ol/liq}\right)$ vs. $10^4/T$(K) showing experiments from this work (downward and upward pointing triangles denoting forward and reverse experiments, respectively) and Matzen et al. (2013) (filled black circles); error bars are propagated from the analytical uncertainties reported in Table 2 (this work) and Table 3 of Matzen et al. (2013). Solid blue line is a weighted least-squares fit to all of the data; dashed blue curves are the 95% confidence interval on the regression. Values of the slope and intercept for the blue line are 3,641 ± 396 and –1.597 ± 0.229, respectively.

Figure 4.

Values of $\ln\left(K_{D,Ni-Mg}^{ol/liq}\right)$ from this study and from the literature (the Filter-B data set from Matzen et al. 2013) plotted as a function of $10^4/T$(K); note that the Filter-B data set includes the experiments reported in Matzen et al. (2013). Solid blue, red, and black lines are fits to three different sets of data: this study + Matzen et al. (filled blue circles; solid blue line is the same as the fit shown in Fig. 3); Filter-B′ = this study + Matzen et al. (filled blue circles) + all other experiments in the Filter-B data set (open and filled gray circles; the fit is shown as a red line); Complex Filter-B′ = this study + Matzen et al. (filled blue circles) + a subset of the Filter-B data, culled so as to only include experiments with liquids containing at least SiO_2, MgO, and ≥ 2 wt. % each of CaO and Al_2O_3 (filled gray circles; the open circles are those literature experiments with < 2 wt. % CaO and/or Al_2O_3 in the glass). Fits to the Filter-B′ and Complex Filter-B′ data sets are based on a robust (iterative, bisquare-weighted, least squares) technique and yield $-\Delta_{r(1)}H^{\circ}_{T_{ref},P_{ref}}/R = 4{,}321 \pm 190$ (K) and $\Delta_{r(1)}S^{\circ}_{T_{ref},P_{ref}}/R = -1.953 \pm 0.115$ (solid red line); $-\Delta_{r(1)}H^{\circ}_{T_{ref},P_{ref}}/R = 4{,}505 \pm 196$ (K) and $\Delta_{r(1)}S^{\circ}_{T_{ref},P_{ref}}/R = -2.075 \pm 0.120$ (solid black line), respectively. The dashed black curves are the 95% confidence bounds on the Complex Filter-B′ fit (for clarity, confidence bounds on the other two fits are not shown).

Figure 5.

Maximum NiO contents of olivine phenocrysts vs. depth to the lithosphere-asthenosphere boundary (km) at the time of eruption (See Table S1). The maximum NiO^{ol} contents for each suite was calculated by substituting the Mg# for the most Mg-rich olivine at a given locality into the equation for a linear or power law fit to the $Mg\#^{ol}$ vs. NiO^{ol} data for that suite; coefficients are reported in Table S2. Sites are differentiated by type of volcanism (tholeiitic, alkalic, or uncertain when the assignment was ambiguous; see notes to Table S1) and by Mg# (greater or less than 90). Values adjacent to the lowest MORB (mid-ocean ridge basalt), Iceland, and Galápagos points are the maximum olivine Mg#s at those three localities. Abbreviations: B = Baffin Bay/Island; D = Detroit seamount (Emperor chain); GC = Gran Canaria (Canary Islands); H-E = Hawaiian-Emperor Chain; I = Iceland; K = Knipovich Ridge; NAIP = North Atlantic igneous province; OIB = ocean island basalt; R = Réunion; S = Suiko seamount (Emperor chain); SM = Sao Migel (Azores); T = Terceria (Azores); WG = West Greenland. Solid line represents calculated enrichments in 1-bar primary olivine phenocrysts using equation (5) and assuming: a 1-bar liquidus temperature of 1356°C, a linear relationship between liquidus temperature and pressure (and depth), and a mantle olivine Ni content of 0.37 wt. %; gray triangular band denotes the effect of using the low and high estimates of 1-bar liquidus temperatures (1266 and 1447°C) calculated from the range of mantle potential temperature estimates (see text); dashed lines represent how variations in mantle olivine NiO (± 0.06 wt. %) affect the 1356°C curve. Tick marks along the top of the figure denote $\Delta T = T_m - T_{1\text{-}bar}$, where T_m is the temperature (and depth) at which the primary melt separates from the mantle; see text for further discussion.

Figure 6.

Calculated maximum olivine NiO contents ($\text{NiO}_{\text{max-Mg\#}}$; based on the regressions in Table S2) vs. the maximum $\text{Mg\#}^{\text{ol}}$ observed at each locality. Only maximum NiO^{ol} values from suites of olivines from tholeiitic lavas are plotted. See text for further discussion.

References

Agee CB, Walker D (1990) Aluminum partitioning between olivine and ultrabasic silicate liquid to 6 GPa. Contrib Mineral Petrol 105:243–254

Albarède F, Provost A (1977) Petrological and geochemical mass-balance equations: an algorithm for least-square fitting and general error analysis. Comput Geosci 3:309–326

Armstrong JT (1988) Quantitative analysis of silicate and oxide minerals: comparison of Monte Carlo, ZAF and ϕ(ρz) procedures. In: Newbury DE (ed) Microbeam Analysis. San Francisco Press, pp 239–246

Arndt NT (1977) Partitioning of nickel between olivine and ultrabasic and basic komatiite liquids. Year Book - Carnegie Institution of Washington (76):553–557

Artemieva, I (2011) The lithosphere: An interdisciplinary approach. Cambridge University Press, 773 pp

Asimow PD, Langmuir CH (2003) The importance of water to oceanic mantle melting regimes. Nature 421:815–820

Baker MB, Alves S, Stolper EM (1996) Petrography and petrology of the Hawaii Scientific Drilling Project lavas: Inferences from olivine phenocryst abundances and compositions. J Geophys Res 101:11715–11727

Beattie P, Ford C, Russell D (1991) Partition coefficients for olivine-melt and orthopyroxene-melt systems. Contrib Mineral Petrol 109:212–224

Beattie P (1993) Olivine-melt and orthopyroxene-melt equilibria. Contrib Mineral Petrol 115:103–111

Berman RG (1983) A thermodynamic model for multicomponent melts, with application to the system CaO-MgO-Al_2O_3-SiO_2. Dissertation, University of British Columbia

Berman RG, Brown TH (1987) Development of models for multicomponent melts: Analysis of synthetic systems. Reviews Mineral 17:405–442

Blundy JD, Falloon TJ, Wood BJ, Dalton JA (1995) Sodium partitioning between clinopyroxene and silicate melts. J Geophys Res 100:15501–15515

Bonatti E, Peyve A, Kepezhinskas P, Kurentsova N, Seyler M, Skolotnev S, Udintsev G (1992) Upper mantle heterogeneity below the mid-Atlantic ridge, 0°-15°N. J Geophys Res 97:4461–4476

Brown EL, Lesher CE (2014) North Atlantic magmatism controlled by temperature, mantle composition and buoyancy. Nature Geosci 7:820–824

Brunelli D, Cipriani A, Ottolini L, Peyve A, Bonatti E (2003) Mantle peridotites from the Bouvet triple junction region, South Atlantic. Terra Nova 15:194–203

Campbell FE, Roeder P (1968) The stability of olivine and pyroxene in the Ni-Mg-Si-O system. Am Mineral 53:257–268

Clague DA, Denlinger RP (1994) Role of olivine cumulates in destabilizing the flanks of Hawaiian volcanoes. Bull Volcanol 56:425–434

Clague DA, Weber WS, Dixon JE (1991) Picritic Glasses from Hawaii. Nature 353:553–556

Coogan LA, Saunders AD, Wilson RN (2014) Aluminum-in-olivine thermometry of primitive basalts: Evidence of an anomalously hot mantle source for large igneous provinces. Chem Geol 368:1–10

Courtier AM, Jackson MG, Lawrence JF, Wang Z, Lee C-TA, Halama R, Warren JF, Workman R, Xu W, Hirschmann MM, Larson AM, Hart SR, Lithgow-Bertelloni C, Stixrude L, Chen W-P (2007) Correlation of seismic and petrologic thermometers suggests deep thermal anomalies beneath hotspots. Earth Planet Sci Lett 264:308–316

Danyushevsky LV, Plechov P (2011) Petrolog3: Integrated software for modeling crystallization processes. Geochem Geophys Geosys 12:Q07021

Dasgupta R, Jackson MG, Lee C-TA (2010) Major element chemistry of ocean island basalts — Conditions of mantle melting and heterogeneity of mantle source. Earth Planet Sci Lett 289:377–392

Edwards SJ, Malpas J (1996) Melt-peridotite interactions in shallow mantle at the East Pacific Rise: evidence from ODP Site 895 (Hess Deep). Mineral Mag 60:191–206

Ellam RM (1992) Lithospheric thickness as a control on basalt geochemistry. Geology 20:153–156

Fram MS, Lesher CE (1993) Geochemical constraints on mantle melting during creation of the North Atlantic basin. Nature 363:712–715

France L, Chazot G, Kornprobst J, Dallai L, Vannucci R, Grégoire M, Bertrand H, Boivin P (2015) Mantle refertilization and magmatism in old orogenic regions: The role of late-orogenic pyroxenites. Lithos 232:49–75

Frei D, Liebscher A, Franz G,Wunder B, Klemme S, Blundy J (2009) Trace element partitioning between orthopyroxene and anhydrous silicate melt on the lherzolite solidus from 1.1 to

3.2 GPa and 1,230 to 1,535°C in the model system Na_2O–CaO–MgO–Al_2O_3–SiO_2. Contrib Mineral Petrol 157:473–490

Gale A, Langmuir CH, Dalton CA (2014) The global systematics of ocean ridge basalts and their origin. J Petrol 55:1051-1082

Garcia MO (1996) Petrography and olivine and glass chemistry of lavas from the Hawaii Scientific Drilling Project. J Geophys Res 101:11701–11713

Geist D, Naumann T, Larson P (1998) Evolution of Galápagos magmas: mantle and crustal fractionation without assimilation. J Petrol 39:953–971

Ghiorso MS, Sack RO (1995) Chemical mass-transfer in magmatic processes IV. A revised and internally consistent thermodynamic model for the interpolation and extrapolation of liquid-solid equilibria in magmatic systems at elevated temperatures and pressures. Contrib Mineral Petrol 119:197–212

Ghose I, Cannat M, Seyler M (1996) Transform fault effect on mantle melting in the MARK area (Mid-Atlantic Ridge south of the Kane transform). Geology 24:1139–1142

Hamlyn PR, Bonatti E (1980) Petrology of mantle-derived ultramafics from the Owen Fracture Zone, Northwest Indian Ocean: Implications for the nature of the oceanic upper mantle. Earth Planet Sci Lett 48:65–79

Harpp KS, White WM, (2001) Tracing a mantle plume: Isotopic and trace element variations of Galápagos seamounts. Geochem Geophys Geosys 2:1042

Hart SR, Davis KE (1978) Nickel partitioning between olivine and silicate melt. Earth Planet Sci Lett 40:203–219

Hellebrand E, Snow JE, Hoppe P, Hofmann AW (2002) Garnet-field melting and late-stage refertilization in 'residual' abyssal peridotites from the central Indian Ridge. J Petrol 43:2305–2338

Hellevang B, Pedersen RB (2005) Magmatic segmentation of the northern Knipovich Ridge: Evidence for high-pressure fractionation at an ultraslow spreading ridge. Geochem Geophys Geosys 6:Q09007

Herzberg C, O'Hara MJ (2002) Plume-associated ultramafic magmas of Phanerozoic age. J Petrol 43:1857–1883

Herzberg C, Asimow PD, Arndt N, Niu Y, Lesher CM, Fitton JG, Cheadle MJ, Saunders AD (2007) Temperatures in ambient mantle and plumes: Constraints from basalts, picrites, and komatiites. Geochem Geophys Geosys 8:Q02006

Herzberg C, Asimow PD (2008) Petrology of some oceanic island basalts: PRIMELT2.XLS software for primary magma calculation. Geochem Geophys Geosys 9:Q09001

Herzberg C, Asimow PD, Ionov DA, Vidito C, Jackson MG, Geist D (2013) Nickel and helium evidence for melt above the core-mantle boundary. Nature 493:393–397

Herzberg C, Asimow PD (2015) PRIMELT3 MEGA.XLSM software for primary magma calculation: Peridotite primary magma MgO contents from the liquidus to the solidus. Geochem Geophys Geosys 16:563–578

Herzberg C, Vidito C, Starkey NA (2016) Nickel-cobalt contents of olivine record origins of mantle peridotite and related rocks. Am Mineral 101:1952–1966

Hirschmann MM, Ghiorso MS (1994) Activities of nickel, cobalt, and manganese silicates in magmatic liquids and applications to olivine/liquid and to silicate/metal partitioning. Geochim Cosmochim Acta 58:4109–4126

Hirschmann MM, Stolper EM (1996) A possible role for garnet pyroxenite in the origin of the "garnet signature" in MORB. Contrib Mineral Petrol 124:185–208

Hofmann AW (2003) Sampling mantle heterogeneity through oceanic basalts: Isotopes and trace elements. In The Mantle and Core (ed Carlson RW) vol 2 Treatise on Geochemistry (eds Holland HD, Turekian KK) pp 61–101

Huang S, Frey FA (2005) Recycled oceanic crust in the Hawaiian plume: evidence from temporal geochemical variations within the Koolau shield. Contrib Mineral Petrol 149:556–575

Ito G, Shen Y, Hirth G, Wolfe CJ (1999) Mantle flow, melting, and dehydration of the Iceland mantle plume. Earth Planet Sci Lett 165:81-96

Iwamori H, McKenzie D, Takahashi E (1995) Melt generation by isentropic mantle upwelling. Earth Planet Sci Lett 134:253–266

Jackson MG, Weis D, Huang S (2012) Major element variations in Hawaiian shield lavas: Source features and perspectives from global ocean island basalt (OIB) systematics. Geochem Geophys Geosys 13:Q09009

Kinzler RJ (1997) Melting of mantle peridotite at pressures approaching the spinel to garnet transition: Application to mid-ocean ridge basalt petrogenesis. J Geophys Res 102:853-874

Kinzler RJ, Grove TL, Recca SI (1990) An experimental study on the effect of temperature and melt composition on the partitioning of nickel between olivine and silicate melt. Geochim Cosmochim Acta 54:1255–1265

Korenaga J, Kelemen PB (2000) Major element heterogeneity in the mantle source of the North Atlantic igneous province. Earth Planet Sci Lett 184:251–268

Lambart S, Laporte D, Schiano P (2013) Markers of the pyroxenite contribution in the major-element compositions of oceanic basalts: Review of the experimental constraints. Lithos 160-161:14–36

Lambart S, Baker MB, Stolper EM (2016) The role of pyroxenite in basalt genesis: Melt-PX, a melting parameterization for mantle pyroxenites between 0.9 and 5 GPa. J Geophys Res Solid Earth 121:5708–5735

Lee C-TA, Luffi P, Plank T, Dalton H, Leeman WP (2009) Constraints on the depths and temperatures of basaltic magma generation on Earth and other terrestrial planets using new thermobarometers for mafic magmas. Earth Planet Sci Lett 279:20–33

Leeman WP, Lindstrom DJ (1978) Partitioning of Ni^{2+} between basaltic and synthetic melts and olivines—an experimental study. Geochim Cosmochim Acta 42:801–816

Li C, Ripley EM (2010) The relative effects of composition and temperature on olivine-liquid Ni partitioning: Statistical deconvolution and implications for petrologic modeling. Chem Geol 275:99–104

Maclennan J (2008) Concurrent mixing and cooling of melts under Iceland. J Petrol 49:1931–1953

Matzen AK, Baker MB, Beckett JR, Stolper EM (2011) Fe-Mg partitioning between olivine and high-magnesium melts and the nature of Hawaiian parental liquids. J Petrol 52:1243-1263

Matzen AK, Baker MB, Beckett JR, Stolper EM (2013) The Temperature and pressure dependence of nickel partitioning between olivine and silicate melt. J Petrol 54:2521–2545

McKenzie D, Bickle MJ (1988) The volume and composition of melt generated by extension of the lithosphere. J Petrol 29:623–679

Médard E, McCammon CA, Barr JA, Grove TL (2008) Oxygen fugacity, temperature reproducibility, and H_2O contents of nominally anhydrous piston-cylinder experiments using graphite capsules. Am Mineral 93:1838–1844

Mysen BO (1978) Experimental determination of nickel partition coefficients between liquid, pargasite, and garnet peridotite minerals and concentration limits of behavior according to Henry's law at high pressure and temperature. Am J Sci 278:217–243

Mysen BO, Kushiro I (1979) Pressure dependence of nickel partitioning between forsterite and aluminous silicate melts. Earth Planet Sci Lett 42:383–388

Nafziger RH, Muan A (1967) Equilibrium phase compositions and thermodynamic properties of olivines and pyroxenes in system MgO-"FeO"-SiO_2. Am Mineral 52:1364–1385

Niu Y, Wilson M, Humphreys ER, O'Hara MJ (2011) The origin of intra-plate ocean island basalts (OIB): the lid effect and its geodynamic implications. J Petrol 52:1443–1468

O’Neill HSC, Eggins SM (2002) The effect of melt composition on trace element partitioning: an experimental investigation of the activity coefficients of FeO, NiO, CoO, MoO_2 and MoO_3 in silicate melts. Chem Geol 186:151–181

O'Neill HSC, Berry AJ (2006) Activity coefficients at low dilution of CrO, NiO and CoO in melts in the system CaO-MgO-Al_2O_3-SiO_2 at 1400°C: Using the thermodynamic behaviour of transition metal oxides in silicate melts to probe their structure. Chem Geol 231:77–89

Pertermann M, Hirschmann MM (2003) Partial melting experiments on a MORB-like pyroxenite between 2 and 3 GPa: Constraints on the presence of pyroxenite in basalt source regions from solidus location and melting rate. J Geophys Res 108:2125

Pouchou J-L, Pichoir F (1988) A simplified version of the "PAP" model for matrix corrections in EPMA. In: Newbury DE (ed) Microbeam Analysis. pp 315–318

Press WH, Teukolsky SA, Vetterling, WT, Flannery BP (1992) Numerical Recipes. Cambridge University Press, Cambridge

Putirka K, Johnson M, Kinzler R, Longhi J, Walker D (1996) Thermobarometry of mafic igneous rocks based on clinopyroxene-liquid equilibria, 0-30 kbar. Contrib Mineral Petrol 123:92–108

Putirka K, Ryerson FJ, Perfit M, Ridley WI (2011) Mineralogy and composition of the oceanic mantle. J Petrol 52:279–313

Putirka KD, Perfit M, Ryerson FJ, Jackson MG (2007) Ambient and excess mantle temperatures, olivine thermometry, and active vs. passive upwelling. Chem Geol 241:177–206

Rampone E, Ramairone A, Hofmann AW (2004) Contrasting bulk and mineral chemistry in depleted mantle peridotites: evidence for reactive porous flow. Earth Planet Sci Lett 218:491–506

Rhodes JM, Vollinger MJ (2004) Composition of basaltic lavas sampled by phase-2 of the Hawaii Scientific Drilling Project: Geochemical stratigraphy and magma types. Geochem Geophys Geosys 5:Q03G13

Richards M, Contreras-Reyes E, Lithgow-Bertelloni C, Ghiorso M, Stixrude L (2013) Petrologic interpretation of deep crustal intrusive bodies beneath oceanic hotspot provinces. Geochem Geophys Geosys 14:604–619

Roeder PL, Emslie RF (1970) Olivine-liquid equilibrium. Contrib Mineral Petrol 29(4):275–289

Ryabchikov ID (2003) High NiO content in mantle-derived magmas as evidence for material transfer from the Earth's core. Dokl Earth Sci 389A:437–439

Sakyi PA, Tanaka R, Kobayashi K, Nakamura E (2012) Inherited Pb isotopic records in olivine antecryst-hosted melt inclusions from Hawaiian lavas. Geochim Cosmochim Acta 95:169–195

Seyler M, Cannat M, Mevel C (2003) Evidence for major-element heterogeneity in the mantle source of abyssal peridotites from the Southwest Indian Ridge (52° to 68° E). Geochem Geophys Geosys 4:9101

Shibata T, Thompson G (1986) Peridotites from the Mid-Atlantic Ridge at 43° N and their petrogenetic relation to abyssal tholeiites. Contrib Mineral Petrol 93:144–159

Shorttle O, Maclennan J, Lambart S (2014) Quantifying lithological variability in the mantle. Earth Planet Sci Lett 395:24–40

Snyder DA, Carmichael ISE (1992) Olivine-liquid equilibria and the chemical activities of FeO, NiO, Fe_2O_3, and MgO in natural basic melts. Geochim Cosmochim Acta 56:303–318

Sobolev AV, Hofmann AW, Kuzmin DV, Yaxley GM, Arndt NT, Chung S-L, Danyushevsky LV, Elliott T, Frey FA, Garcia MO, Gurenko AA, Kamenetsky VS, Kerr AC, Krivolutskaya NA, Matvienkov VV, Nikogosian IK, Rocholl A, Sigurdsson IA, Sushchevskaya NM, Teklay M (2007) The amount of recycled crust in sources of mantle-derived melts. Science 316:412–417

Sobolev AV, Hofmann AW, Sobolev SV, Nikogosian IK (2005) An olivine-free mantle source of Hawaiian shield basalts. Nature 434:590–597

Stephens CJ (1997) Heterogeneity of oceanic peridotite from the western canyon wall at MARK: Results from site 920. In: Karson JA, Cannat M, Miller DJ, Elthon D (eds) Proc ODP Sci Results 153: College Station TX (Ocean Drilling Program), pp 285–303

Stolper E, Sherman S, Garcia M, Baker M, Seaman C (2004) Glass in the submarine section of the HSDP2 drill core, Hilo, Hawaii. Geochem Geophys Geosys 5:Q07G15

Stolper E, Asimow P (2007) Insights into mantle melting from graphical analysis of one-component systems. Am J Sci 307:1051–1139

Sugawara T (2000) Empirical relationships between temperature, pressure, and MgO content in olivine and pyroxene saturated liquid. J Geophys Res 105:8457–8472

Takahashi E (1978) Partitioning of Ni^{2+}, Co^{2+}, Fe^{2+}, Mn^{2+} and Mg^{2+} between olivine and silicate melts: compositional dependence of partition coefficient. Geochim Cosmochim Acta 42:1829–1844

Thomson A, Maclennan J (2013) The distribution of olivine compositions in Icelandic basalts and picrites. J Petrol 54:745–768

Toplis MJ (2005) The thermodynamics of iron and magnesium partitioning between olivine nad liquid: criteria for assessing and predicting equilibrium in natural and experimental systems. Contrib Mineral Petrol 149:22–39

Vidito C, Herzberg C, Gazel E, Geist D, Harpp K (2013) Lithological structure of the Galápagos plume. Geochem Geophys Geosys 14:4214–4240

Wang Z, Gaetani GA (2008) Partitioning of Ni between olivine and siliceous eclogite partial melt: experimental constraints on the mantle source of Hawaiian basalts. Contrib Mineral Petrol 156:661–678

Warren JM, Shimizu N (2010) Cryptic variations in abyssal peridotite compositions: Evidence for shallow-level melt infiltration in the oceanic lithosphere. J Petrol 51:395–423

Winpenny B, Maclennan J (2011) A Partial Record of Mixing of Mantle Melts Preserved in Icelandic Phenocrysts. J Petrol 52:1791–1812

Wood BJ, Wade J (2013) Activities and volatilities of trace components in silicate melts: a novel use of metal–silicate partitioning data. Contrib Mineral Petrol 166:911–921

Figure 1

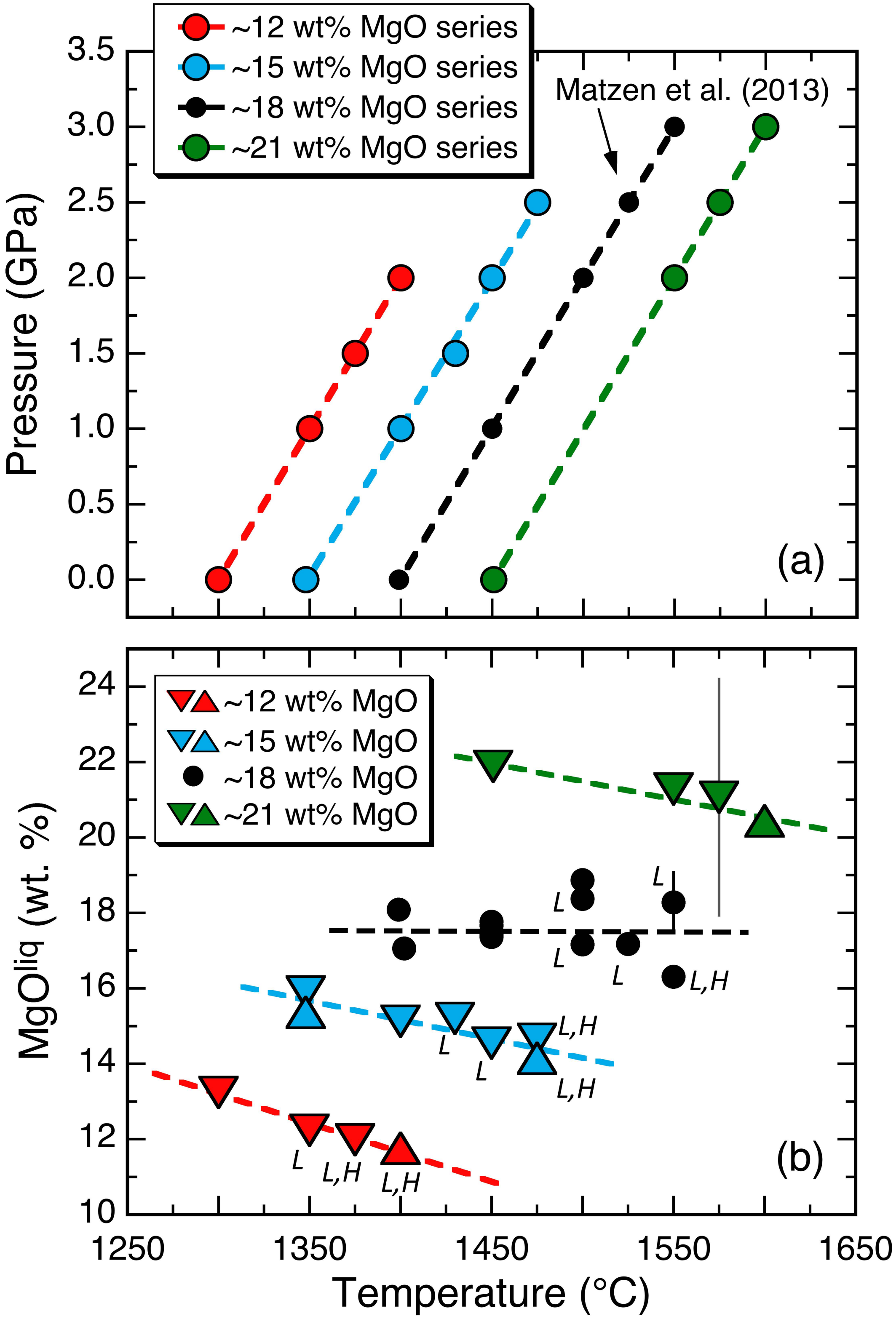

~12 wt% MgO series
~15 wt% MgO series
~18 wt% MgO series
~21 wt% MgO series
Matzen et al. (2013)
Pressure (GPa)
3.5
3.0
2.5
2.0
1.5
1.0
0.5
0.0
(a)
~12 wt% MgO
~15 wt% MgO
~18 wt% MgO
~21 wt% MgO
MgO^{liq} (wt. %)
24
22
20
18
16
14
12
10
L
L,H
(b)
1250
1350
1450
1550
1650
Temperature (°C)

Figure 2

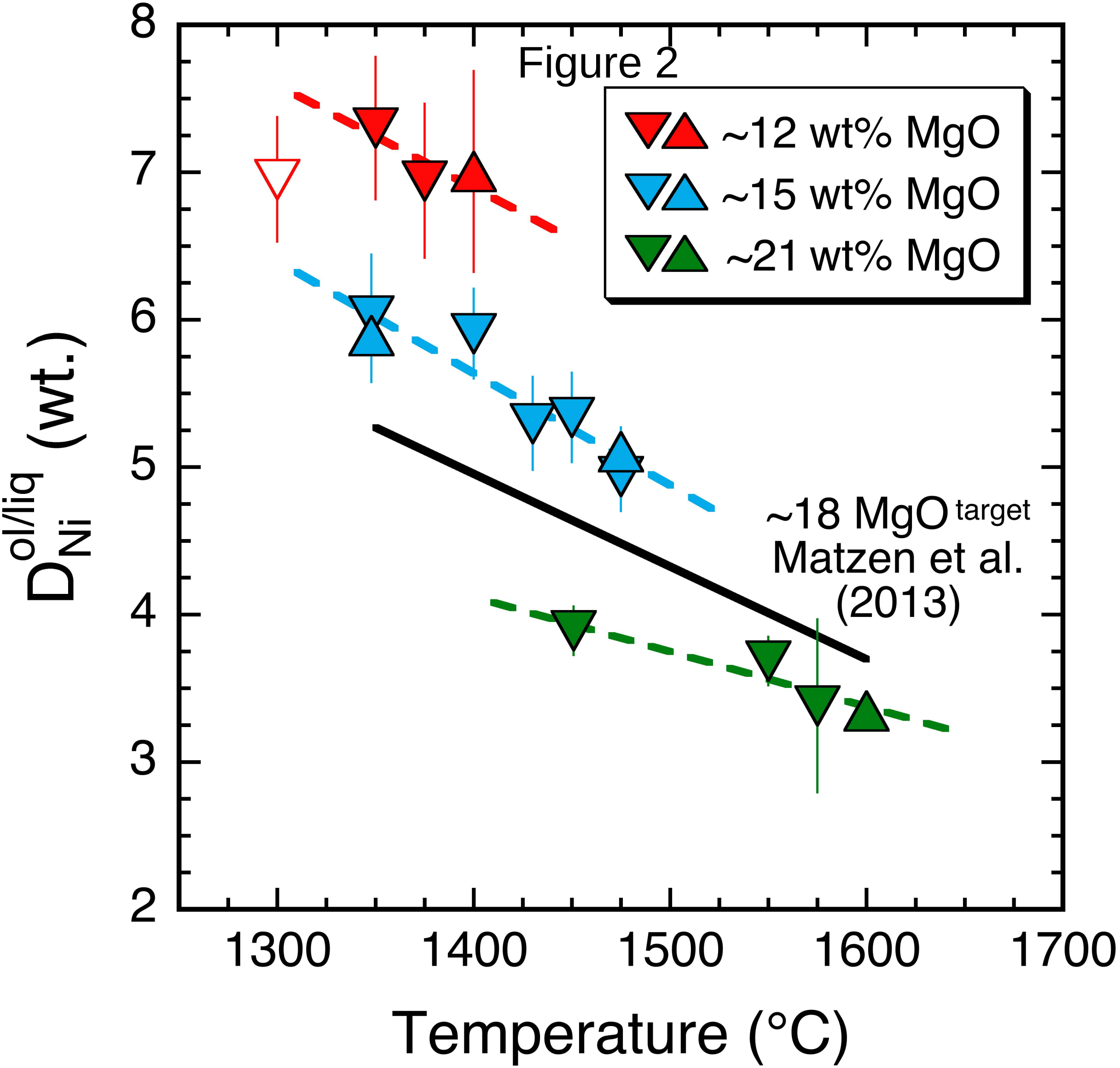

🟥 ~12 wt% MgO
🟦 ~15 wt% MgO
🟩 ~21 wt% MgO
~18 MgO target
Matzen et al.
(2013)
$D_{Ni}^{ol/liq}$ (wt.)
8
7
6
5
4
3
2
1300
1400
1500
1600
1700
Temperature (°C)

Figure 3

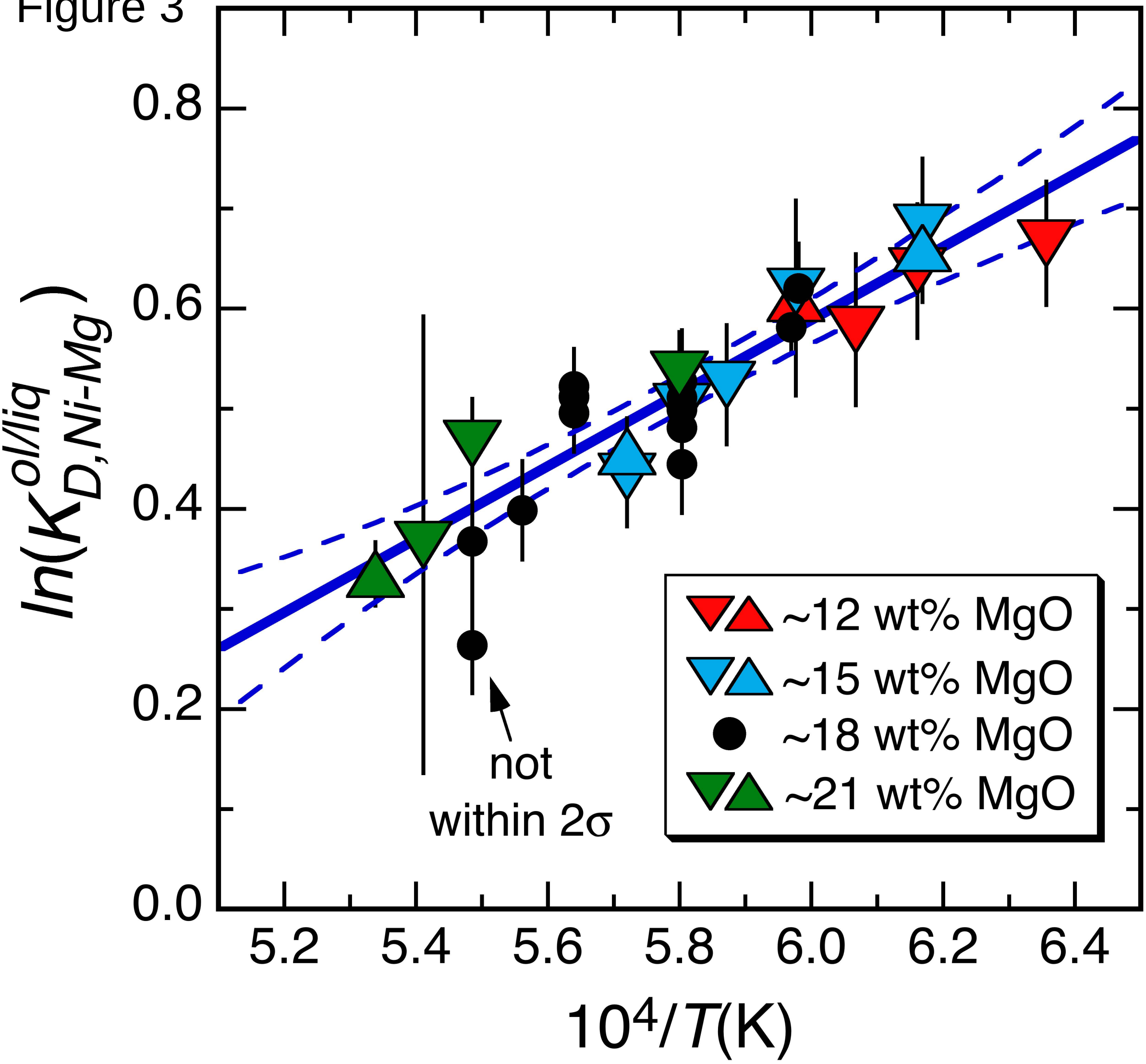
0.8
0.6
0.4
0.2
0.0
$ln(K^{ol/liq}_{D,Ni\text{-}Mg})$
5.2
5.4
5.6
5.8
6.0
6.2
6.4
$10^4/T$(K)
▼▲ ~12 wt% MgO
▼▲ ~15 wt% MgO
● ~18 wt% MgO
▼▲ ~21 wt% MgO
not within 2σ

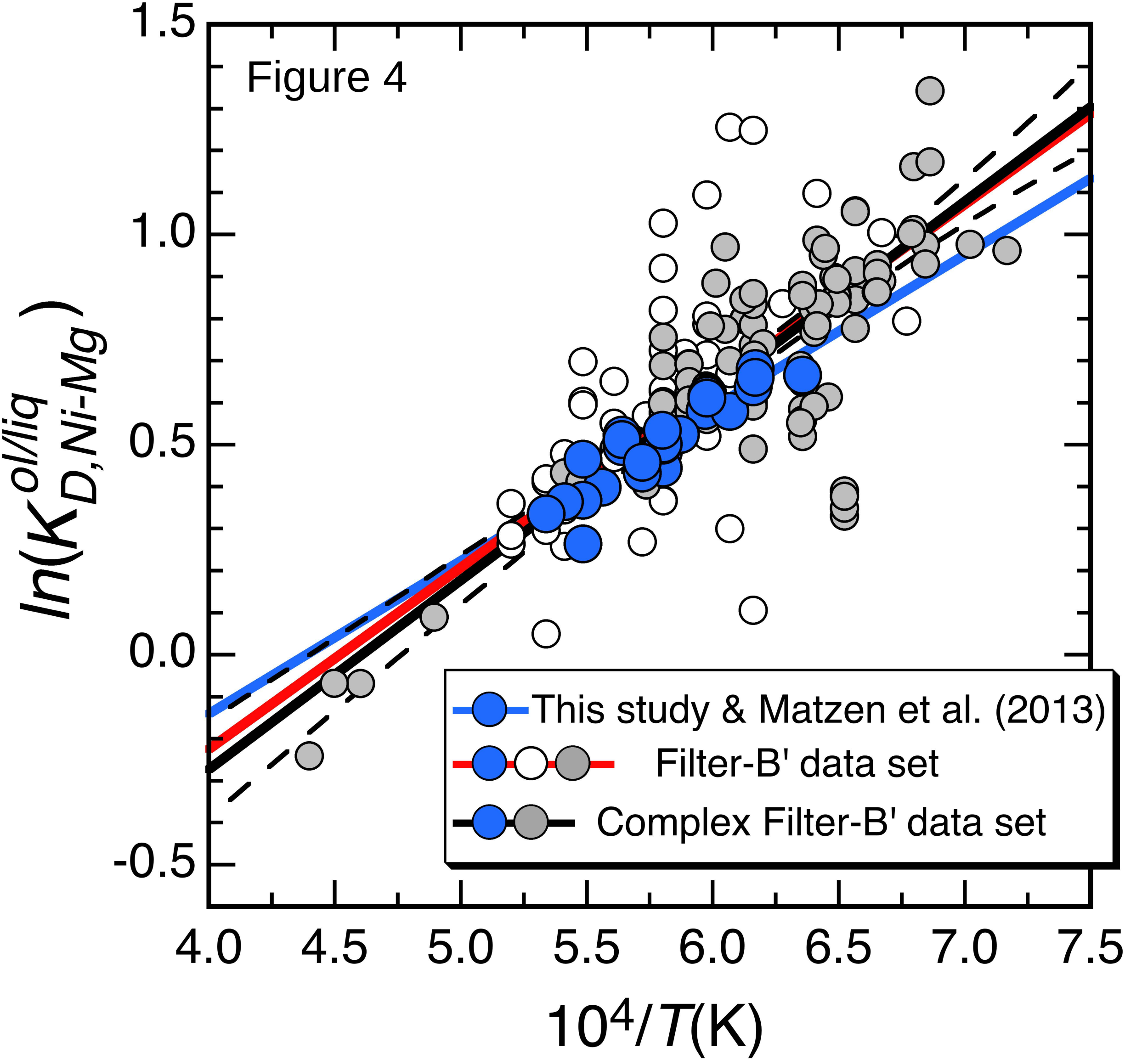

Figure 4

1.5
1.0
0.5
0.0
-0.5
$ln(K_{D,Ni-Mg}^{ol/liq})$
4.0
4.5
5.0
5.5
6.0
6.5
7.0
7.5
$10^4/T(K)$
This study & Matzen et al. (2013)
Filter-B' data set
Complex Filter-B' data set

Figure 5

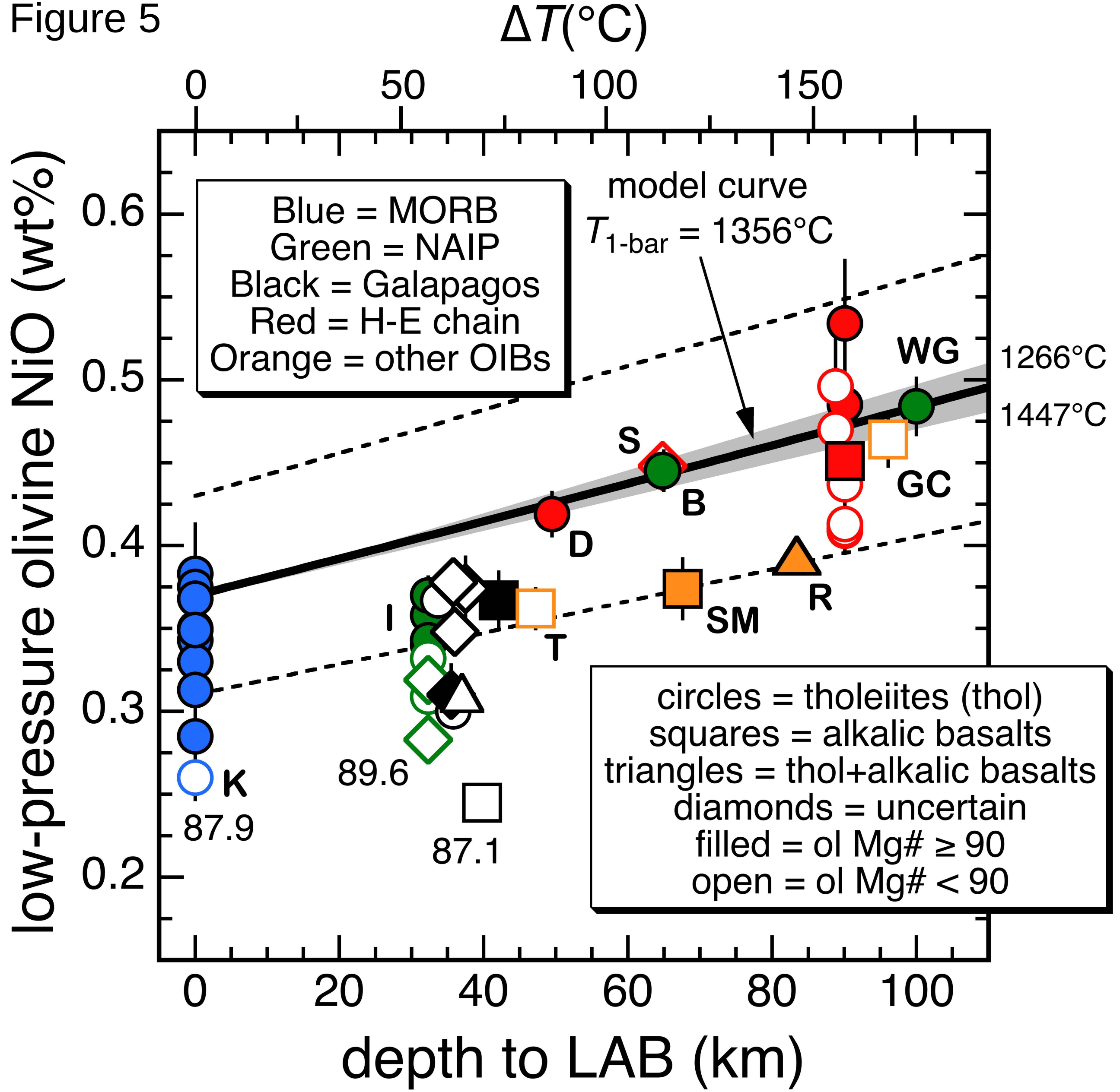
ΔT(°C)
0
50
100
150
model curve
$T_{1\text{-bar}}$ = 1356°C
Blue = MORB
Green = NAIP
Black = Galapagos
Red = H-E chain
Orange = other OIBs
1266°C
1447°C
WG
S
B
GC
D
I
T
SM
R
K
87.9
89.6
87.1
circles = tholeiites (thol)
squares = alkalic basalts
triangles = thol+alkalic basalts
diamonds = uncertain
filled = ol Mg# ≥ 90
open = ol Mg# < 90
low-pressure olivine NiO (wt%)
0.6
0.5
0.4
0.3
0.2
0
20
40
60
80
100
depth to LAB (km)

Figure 6

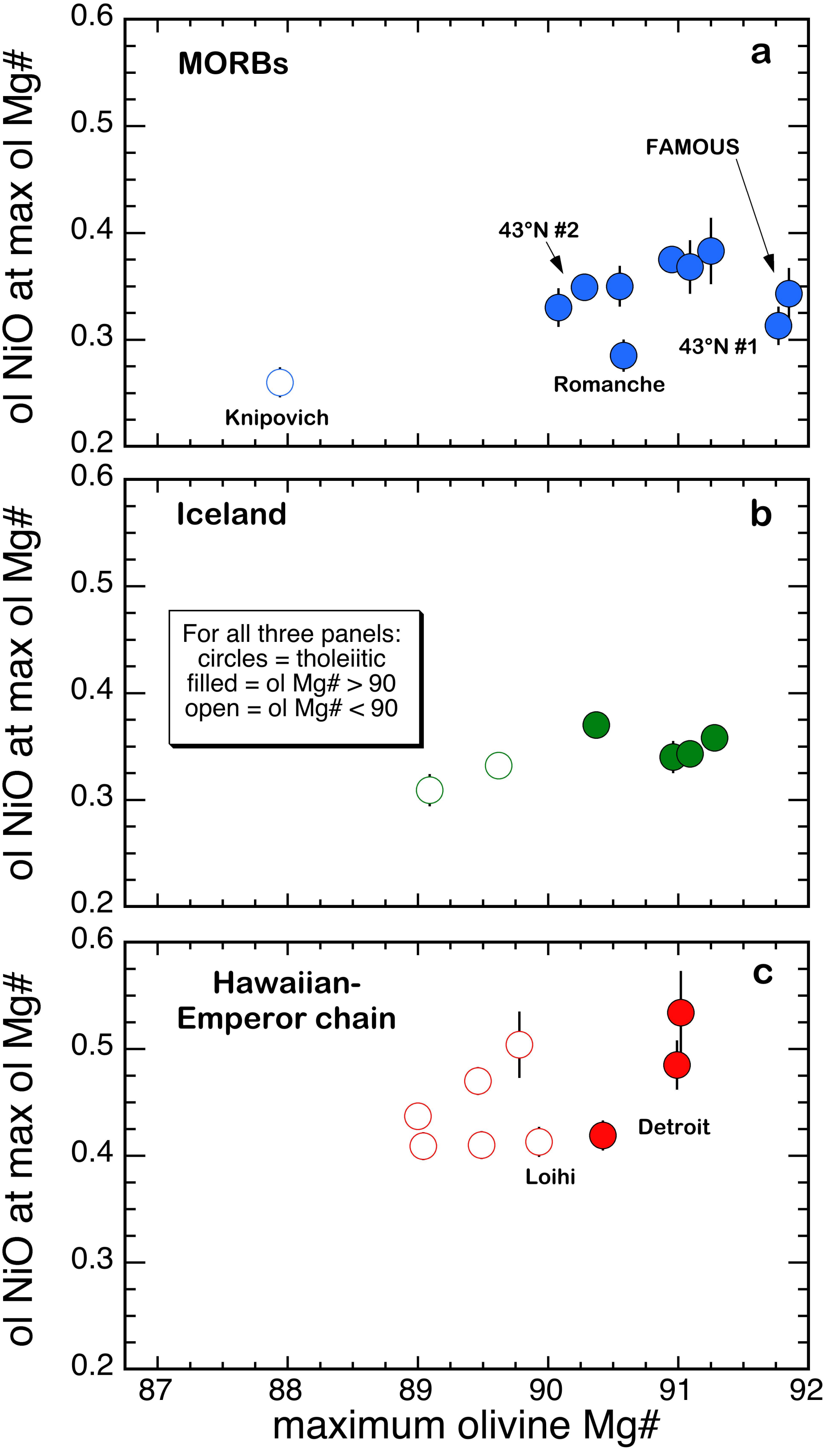

MORBs
a
FAMOUS
43°N #2
43°N #1
Romanche
Knipovich
Iceland
b
For all three panels:
circles = tholeiitic
filled = ol Mg# > 90
open = ol Mg# < 90
Hawaiian-
Emperor chain
c
Detroit
Loihi
ol NiO at max ol Mg#
0.2
0.3
0.4
0.5
0.6
87
88
89
90
91
92
maximum olivine Mg#

Table 1. Run Conditions and Run Products

Run #	Series	Final Run Conditions			Hot Press Conditions			Capsule[a]	Initial Glass[b] (wt. %)	Run Products[c]	Phase Proportions[d] (wt. %)	% NiO Change[e] (relative)	Q-value[f]	$D_{Ni}^{ol/liq}$ [g]
		T(°C)	P(GPa)	t(hrs)	T(°C)	P(GPa)	t(hrs)							
49	15	1430	1.5	12.0	915	1.40	5.8	Pt-C	5.09	gl, ol, l-px	43.7, 52.9, 3.4	+1.3	0.87	5.30(33)
50	15	1450	2.0	12.1	940	1.74	6.0	Pt-C	6.28	gl, ol, l-px	49.2, 36.0, 14.8	+2.1	1.97	5.34(29)
51[h]	15	1400	1.0	12.0	915	1.40	6.0	Pt-C	4.51	gl, ol	38.0, 62.0	–0.6	0.07	5.91(34)
52	12	1375	1.5	12.0	915	1.38	6.3	Pt-C	2.47	gl, ol, l-px, h-px	49.8, 35.1, 2.4, 12.7	+1.7	1.00	6.94(46)
53	12	1350	1.0	12.2	915	1.40	6.7	Pt-C	3.19	gl, ol, l-px	45.1, 52.8, 2.1	+1.1	0.68	7.29(52)
56	15	1475	2.5	12.0	965	2.20	5.9	Pt-C	1.78	gl, ol, l-px, h-px	41.1, 30.3, 7.5, 21.0	+1.5	0.99	4.94(25)
58	21	1550	2.0	12.0	940	1.74	6.0	Pt-C	1.59	gl, ol	5.3, 94.7	–4.2	1.00	3.69(16)
59	21	1575	2.5	12.0	965	2.20	6.0	Pt-C	1.08	gl[i], ol	13.4, 86.6	+1.1	1.00	3.38(59)
62R	12	1400	2.0	12.0	940	1.70	6.2	Pt-C	0.96	gl, ol, l-px, h-px	32.9, 35.5, 7.2, 24.3	-	1.00	7.01(69)
63R	15	1475	2.5	12.2	965	2.23	6.0	Pt-C	2.13	gl, ol, l-px, h-px	41.7, 29.1, 4.2, 25.0	-	1.00	5.10(17)
64R	21	1600	3.0	12.0	990	2.65	6.2	Pt-C	3.81	gl, ol	13.6, 86.4	-	0.88	3.35(11)
65	15	1348	1×10^{-4}	12.1	-	-	-	SCOl	–8.63	gl, ol	78.7, 21.3	–11.5	0.47	6.03(38)
67R	15	1348	1×10^{-4}	12.2	-	-	-	SCOl	–8.63	gl, ol	82.8, 17.2	-	0.55	5.89(31)
68	12	1300	1×10^{-4}	11.5	-	-	-	SCOl	–9.16	gl, ol	78.3, 21.7	–4.7	0.69	6.95(44)
70	21	1451	1×10^{-4}	8.1	-	-	-	SCOl	–7.66	gl, ol	51.4, 48.6	–6.2	0.57	3.89(17)

Note: Run number followed by the letter R denotes a reversal experiment. Relative change in bulk Na_2O for one-atmosphere experiments, runs 65, 67R, 68, and 70, are –15.5, –15.1, –13.8, and –16.2 percent, respectively. Hot press conditions are not applicable to the 1-atm experiments.

[a] Capsule abbreviations: Pt-C, platinum-graphite double capsule; SCOl, San Carlos Olivine.

[b] Value listed for one-atmosphere experiments is the measured $\log_{10} fO_2$.

[c] Run products abbreviations: gl = glass (quenched liquid) or a quench mat, ol = olivine, l-px = low-Ca pyroxene, h-px = higher-Ca pyroxene.

[d] Phase proportions, calculated by mass balance, are given in the same order as listed in the run products column. Calculated pyroxene proportions correspond to the order in which they appear in Table 3.

[e] Relative change (in percent) of NiO from the bulk composition based on mass balance; negative sign denotes a decrease while a positive sign indicates an increase in the NiO content of the bulk. Values are not reported for the reversal experiments where NiO in the olivine is strongly zoned towards the rims leading to values that are a numerical artifact of this zoning (see text for further discussion).

[f] Goodness of fit measure, values above 0.05 indicate a solutions acceptable at the 95% confidence level.

[g] Measured olivine-liquid Ni partition coefficient, by weight. Number enclosed in parentheses represents the analytical uncertainty according to the least units cited, e.g., 5.30(33) represents5.30 ± 0.33. Error reflects the propagated analytical uncertainty (one sample standard deviation) of NiO in the olivine and glass (Table 2).

[h] Upon heating to the final-run temperature, pressure increased above the desired final-run pressure. Pressure was slowly bled off until final run-pressure was reached. Thus, this experiment was hot-piston out; all other runs were hot-piston in.

[i] Quench mat.

Table 2. Phase Compositions

Run #	Phase	n	SiO_2	TiO_2	Al_2O_3	Cr_2O_3	FeO	MnO	MgO	CaO	Na_2O	K_2O	P_2O_5	NiO[a]	Total
49	liq	10	48.71(14)	1.68(2)	12.23(5)	0.028(2)	10.14(7)	0.20(3)	15.21(8)	9.27(5)	2.34(3)	0.15(1)	0.16(2)	0.070(4)	100.18
49	ol	10	40.53(8)	0.017(5)	0.075(3)	0.017(3)	11.05(8)	0.154(4)	47.69(7)	0.26(1)	-	-	-	0.371(6)	100.17
49	l-px	6	55.77(18)	0.18(3)	2.79(9)	0.082(12)	7.16(28)	0.15(2)	31.77(26)	1.79(8)	0.09(1)	bdl	bdl	0.14(2)	99.93
50	liq	10	46.44(8)	1.86(3)	12.58(7)	0.022(1)	11.05(8)	0.19(2)	14.55(6)	10.04(4)	2.54(3)	0.17(1)	0.18(2)	0.072(4)	99.68
50	ol	10	40.40(15)	0.016(4)	0.09(2)	0.012(4)	11.76(13)	0.158(6)	47.02(26)	0.29(2)	-	-	-	0.386(5)	100.14
50	l-px	8	55.00(41)	0.19(2)	4.16(51)	0.070(18)	7.28(14)	0.16(2)	30.12(37)	2.44(7)	0.19(1)	bdl	bdl	0.16(3)	99.77
51	liq	10	49.98(11)	1.59(2)	12.01(11)	0.028(1)	9.93(8)	0.175(12)	15.13(7)	8.69(3)	2.21(3)	0.141(5)	0.15(2)	0.063(3)	100.10
51	ol	10	40.76(6)	0.021(6)	0.049(5)	0.018(3)	10.79(5)	0.149(7)	48.22(17)	0.25(1)	-	-	-	0.369(7)	100.62
52	liq	10	48.11(8)	1.93(1)	14.12(9)	0.022(1)	10.49(6)	0.167(13)	11.99(5)	10.35(4)	2.86(6)	0.19(1)	0.19(3)	0.054(4)	100.46
52	ol	6	40.47(7)	0.015(9)	0.06(2)	0.014(4)	12.81(24)	0.174(6)	46.63(17)	0.26(4)	-	-	-	0.371(3)	100.80
52	l-px	8	54.48(35)	0.26(4)	3.93(61)	0.082(19)	8.31(14)	0.17(3)	29.69(32)	2.50(12)	0.15(3)	bdl	bdl	0.11(2)	99.69
52	h-px	13	54.66(62)	0.24(6)	3.29(81)	0.084(22)	8.21(35)	0.21(3)	26.42(1.04)	6.18(96)	0.35(5)	bdl	bdl	0.11(3)	99.76
53	liq	15	50.06(11)	1.78(3)	13.56(11)	0.025(2)	9.29(10)	0.17(2)	12.24(10)	10.12(5)	2.57(3)	0.16(1)	0.16(3)	0.049(3)	100.18
53	ol	10	40.62(9)	0.018(6)	0.05(1)	0.018(2)	11.95(10)	0.166(5)	47.23(20)	0.27(3)	-	-	-	0.358(9)	100.67
53	l-px	2	56.16(60)	0.20(5)	2.15(58)	0.098(9)	8.15(5)	0.177(5)	31.01(5)	2.11(3)	0.08(2)	bdl	bdl	0.13(2)	100.28
56	liq	10	44.81(15)	2.23(4)	12.96(6)	0.016(1)	12.06(7)	0.19(2)	14.65(7)	9.24(4)	2.73(4)	0.20(1)	0.22(3)	0.078(3)	99.39
56	ol	7	40.52(18)	0.027(3)	0.13(2)	0.008(3)	12.23(60)	0.154(6)	46.96(61)	0.26(2)	-	-	-	0.387(11)	100.69
56	l-px	10	53.43(39)	0.23(2)	6.01(51)	0.047(9)	7.74(18)	0.16(1)	29.31(31)	2.38(32)	0.28(4)	bdl	bdl	0.13(3)	99.74
56	h-px	7	52.58(42)	0.32(6)	6.41(55)	0.053(11)	7.38(32)	0.19(3)	23.41(70)	7.97(64)	0.85(5)	bdl	bdl	0.11(2)	99.30
58	liq	7	48.12(13)	1.23(2)	9.12(8)	0.027(1)	11.50(13)	0.22(3)	21.29(10)	6.33(5)	1.59(5)	0.121(5)	0.10(2)	0.096(2)	99.74
58	ol	10	41.03(8)	0.011(5)	0.084(3)	0.015(2)	9.61(3)	0.131(6)	49.28(9)	0.17(1)	-	-	-	0.355(14)	100.70
59	liq[b]	10	48.03(88)	1.31(15)	9.55(98)	0.025(1)	11.56(29)	0.22(2)	21.07(3.13)	6.85(86)	1.60(15)	0.12(1)	0.11(3)	0.111(19)	100.57
59	ol	10	41.24(8)	0.012(6)	0.10(1)	0.011(2)	9.57(3)	0.132(5)	49.50(7)	0.19(1)	-	-	-	0.375(10)	101.13
62R	liq	9	45.15(10)	2.54(3)	14.83(6)	0.015(4)	11.05(9)	0.16(3)	11.76(7)	9.15(4)	3.46(11)	0.27(1)	0.28(2)	0.232(11)	98.90
62R	ol	8	39.90(11)	0.031(5)	0.12(3)	0.010(3)	13.32(21)	0.168(5)	44.75(25)	0.27(1)	-	-	-	1.625(138)	100.18
62R	l-px	8	52.38(50)	0.41(9)	6.83(60)	0.052(21)	8.66(42)	0.16(1)	27.60(74)	2.50(56)	0.28(7)	bdl	bdl	0.64(8)	99.56
62R	h-px	12	51.12(34)	0.52(10)	7.54(38)	0.062(20)	7.93(45)	0.20(3)	19.72(96)	10.39(76)	0.92(6)	bdl	bdl	0.66(25)	99.10
63R	liq	9	44.38(10)	2.33(4)	13.15(6)	0.010(1)	12.01(7)	0.19(2)	14.15(7)	9.20(5)	2.82(5)	0.22(1)	0.27(4)	0.279(6)	99.00
63R	ol	7	40.36(8)	0.033(8)	0.13(3)	0.006(4)	12.75(6)	0.157(6)	45.70(11)	0.28(1)	-	-	-	1.425(35)	100.85
63R	l-px	9	53.25(72)	0.26(4)	6.34(70)	0.030(12)	7.87(17)	0.16(2)	28.75(40)	2.24(14)	0.28(2)	bdl	bdl	0.56(4)	99.76
63R	h-px	8	52.58(61)	0.32(6)	6.69(92)	0.054(24)	7.91(41)	0.20(3)	21.87(89)	8.23(77)	0.94(5)	bdl	bdl	0.73(7)	99.56
64R	liq	10	46.74(13)	1.40(2)	9.64(7)	0.024(2)	11.60(5)	0.21(3)	20.45(8)	7.44(4)	1.70(3)	0.127(4)	0.15(2)	0.197(3)	99.67
64R	ol	10	41.00(11)	0.016(6)	0.14(1)	0.012(2)	9.69(2)	0.133(4)	48.94(15)	0.225(4)	-	-	-	0.660(18)	100.82
65	liq	10	48.92(14)	1.56(3)	11.48(8)	0.027(1)	11.31(9)	0.20(3)	15.91(6)	8.99(5)	1.76(4)	0.10(1)	0.13(3)	0.062(4)	100.45
65	ol	10	40.98(9)	0.017(8)	0.019(5)	0.024(4)	10.77(4)	0.153(7)	48.52(12)	0.22(3)	-	-	-	0.373(9)	101.09
67R	liq	10	48.91(10)	1.55(3)	11.41(4)	0.028(2)	11.55(7)	0.20(2)	15.37(7)	9.05(5)	1.81(2)	0.11(1)	0.14(2)	0.370(5)	100.49
67R	ol	9	40.57(13)	0.017(4)	0.021(8)	0.027(3)	10.88(6)	0.155(5)	46.78(22)	0.24(2)	-	-	-	2.178(113)	100.86
68	liq	10	49.72(17)	1.71(4)	12.42(6)	0.027(2)	11.09(7)	0.20(2)	13.24(6)	9.71(7)	1.95(3)	0.12(1)	0.14(3)	0.052(3)	100.37

68	ol	10	40.68(19)	0.020(5)	0.017(6)	0.021(2)	12.03(35)	0.171(7)	47.33(45)	0.22(5)	-	-	-	0.361(7)	100.84
70	liq	10	47.28(14)	1.27(2)	9.24(7)	0.029(1)	11.64(4)	0.20(2)	21.89(12)	7.28(5)	1.42(3)	0.07(1)	0.11(3)	0.102(4)	100.52
70	ol	4	41.22(5)	0.008(6)	0.040(2)	0.019(1)	8.74(10)	0.123(8)	49.93(9)	0.22(1)	-	-	-	0.396(6)	100.70

Note: All compositions listed in wt. %. Phase abbreviations as in Table 1. Numbers in parentheses are analytical uncertainties in terms of the least units cited, e.g., 48.71(14) corresponds to 48.71±0.14 where 48.71 represents the average of n analyses, and 0.14 is one standard deviation of those analyses; when the error is ≥1.0, we include the decimal point. FeO* = all Fe as FeO. Dashed line indicates that the element was not analyzed, bdl = below detection limit.

[a] Element in glass phase analyzed with a 200 nA beam current. n for concentrations in the glass for these elements are 12 for Run 75; 9 for Runs 50 and 53; 7 for Runs 61, and 62R; 5 for Runs 55 and 58; and 10 for all others.

[b] Quench mat.

Supplemental Material to the paper “The effect of liquid composition on the partitioning of Ni between olivine and silicate melt”

Andrew K. Matzen, Michael B. Baker, John R. Beckett, Bernard J. Wood, and Edward M. Stolper

Evaluating deviations in $D_{Ni}^{ol/liq}$ for each of the MgO series

All of our experimental data from this study were used in global fits to equation (3) in the main text but we also examined series of experiments with roughly constant liquid compositions. However, as discussed in the main text, our choice of temperature and pressure for an experiment did not always produce a liquid composition with an MgO content that overlapped that of the target value ($MgO^{liq,target}$ = 12, 15, or 21 wt%, this study; or 18 wt% for Matzen et al. 2013). Since the effect of temperature on $D_{Ni}^{ol/liq}$ in each set of constant MgO experiments (the slope of the best-fit line in $D_{Ni}^{ol/liq}$ vs. T(°C) space for each of the series) can only be evaluated if variations in $D_{Ni}^{ol/liq}$ due to liquid composition (e.g., Hart and Davis 1978) are small, it is necessary to evaluate how deviations from $MgO^{liq,target}$ (and variations in olivine Mg#) among the experiments in a given series generate systematic offsets in the Ni partition coefficients. In practice, this means that runs with a relatively large deviation from the target MgO content should be excluded from the regression for that set of constant wt% MgO experiments.

To evaluate whether or not a compositional deviation was too large for an experiment to be assigned to one of the constant composition series, we compared, for each experiment, $D_{Ni,meas}^{ol/liq}$ (= NiO^{ol}/NiO^{liq}) to $D_{Ni,target}^{ol/liq}$ (= $\exp[3641/T(\mathrm{K}) - 1.597 - \ln(MgO^{liq,target}/MgO^{ol})]$) where 3641 and –1.597 are the $-\Delta H/R$ and $\Delta S/R$ values from the weighted fit to all data from this study and Matzen et al. (2013), and NiO and MgO values for each phase are in wt%. Given observed variations in liquid MgO content and olivine Mg# within each set of constant MgO-series experiments, it's easy to show that variations in MgO^{liq} exert a much larger effect on $D_{Ni}^{ol/liq}$ than do observed variations in olivine composition. Thus, the difference between $D_{Ni,target}^{ol/liq}$ and $D_{Ni,meas}^{ol/liq}$ shows how deviations in MgO content of the liquid from the target value in each experiment influence $D_{Ni}^{ol/liq}$. Only for run 68 (this study) is $\left|D_{Ni,target}^{ol/liq} - D_{Ni,meas}^{ol/liq}\right|$ larger than twice the uncertainty calculated for the experimental $D_{Ni,meas}^{ol/liq}$ value using the mean fractional error calculated from all 28 $D_{Ni,meas}^{ol/liq}$ values (this study and Matzen et al. 2013) and their associated standard deviations. This approach of using a mean fractional error generates a standard deviation for each experimental $D_{Ni,meas}^{ol/liq}$ that reflects the precision of the entire data set. The large value of $\left|D_{Ni,target}^{ol/liq} - D_{Ni,meas}^{ol/liq}\right|$ for run 68, 1.13, compared to its calculated standard deviation of 0.39, is the reason that it was not included in the regression of the ~12 wt% MgO series experiments (Fig. 2, main text).

Predictive models for $D_{Ni}^{ol/liq}$

An important characteristic for any predictive model is its ability to reproduce the data used in its construction. Recently, Herzberg et al. (2013, 2014) compared some of the available models of $D_{Ni}^{ol/liq}$ and concluded that a Jones-Beattie-type model (e.g., Jones 1984; Beattie et al. 1991) recovered the experimental data with the smallest error. To arrive at this conclusion, Herzberg et al. (2013) used a sum-of-squares statistic, $\sqrt{\frac{\sum\left(D_{Ni,calc}^{ol/liq} - D_{Ni,meas}^{ol/liq}\right)^2}{N-1}}$, where N is the number of experiments considered. This statistic is highly vulnerable to outliers and computed deviations are weighted on an absolute, not relative, basis, making it more sensitive to high $D_{Ni}^{ol/liq}$ values than low ones.

After the addition of the new work presented here, our un-filtered experimental database contains 463 experiments, a significant increase compared to the 271 experiments compiled by Herzberg et al. (2013). Only ~40% of the 463 experiments passed our filtering tests, suggesting that Herzberg et al. (2013) may have used a noisier data set. For these reasons, we calculated relative percent errors (defined as, $100 \times \left| D_{Ni,calc}^{ol/liq} - D_{Ni,meas}^{ol/liq} \right| / D_{Ni,meas}^{ol/liq}$ where the vertical bars denote absolute value) for the Jones-Beattie model and equation (3) from the present study using the entire Filter B′ data set (as opposed to the edited data set discussed in the main text, so as to provide a more stringent test). For the Jones-Beattie model, we used two sets of parameters; one as given by Beattie et al. (1991), and a second obtained by refitting the Filter B′ data set using their model. Both equation (3) from this study and the Beattie et al. equation were fit using the same robust technique and $D_{Ni}^{ol/liq}$ values were calculated using single-cation mole-fraction liquid and olivine compositions; average percent errors for the three fits are: 11.3, equation (3); 18.1, Beattie et al. (1991); 14.9, Beattie et al. (1991), refit.

Figure S1 shows the fraction of experiments from the Filter B′ data set whose error on the calculated partition coefficient is less than, or equal to, a given percent error. A superior predictive model will include a larger fraction of experiments at any given error, especially for those data points with the smallest errors (i.e., it will plot above other models in Fig. S1). In this study and in Matzen et al. (2013), careful microprobe work led to ~5% uncertainties on our measured $D_{Ni}^{ol/liq}$ s; we take this to be a rough estimate of the errors expected when analytical uncertainties are minimized and, thus, a model that reproduces all experimentally-measured partition coefficients within ~5% would be viewed as a complete success. As shown in Fig. S1, using equation (3), 37% of the 183 experiments in the Filter-B′ data set have calculated $D_{Ni}^{ol/liq}$ s within 5% of their measured values (for the 28 experiments from this study and Matzen et al. (2013) the value is 54%). Despite having the same number of fit parameters (two), the performance of the Jones-Beattie model is not as good; only ~20% of the experiments have calculated $D_{Ni}^{ol/liq}$ s within 5% of measured values using coefficients reported by Beattie et al. (1991). This rises to ~25% if their coefficients are refit using the Filter-B′ data set, still well below the 37% achieved using equation (3). The superior performance of the temperature-dependent exchange-reaction model is not limited to the lowest percent errors; at any given percent error below 42%, the exchange-reaction model successfully reproduces more of the data set (at least up to ~97% of the data) than does the Jones-Beattie-type approach.

Another way to judge model performance is by asking what percent error on $D_{Ni}^{ol/liq}$ is needed to account for a certain fraction of experiments in the database. For example, to account for 80% of the experiments in the database using the temperature-dependent exchange reaction requires an error on $D_{Ni}^{ol/liq}$ of 16%, whereas the Jones-Beattie approach (using the coefficients from Beattie et al. 1991) requires a substantially larger error on $D_{Ni}^{ol/liq}$, 28% (using the refit coefficients and the Jones-Beattie equation, the required error is ~22%). The Filter-B′ data set contains experiments with similar $D_{Mg}^{ol/liq}$ values but different $D_{Ni}^{ol/liq}$ values (due to the temperature dependence of $D_{Ni}^{ol/liq}$), and thus some of the error associated with the Jones-Beattie equation seen in Fig. S1 may reflect this mix of 1-atm and high-pressure experiments. Figure S2 shows % error vs. cumulative fraction for robust fits to equation (3), this study, and the Jones-Beattie equation using only the 136 1-atm experiments in the Filter-B′ data set. Again, equation

(3), this study, fits a larger fraction of the data at relatively low errors than does the Jones-Beattie model.

Finally, although the correlation between $D_{Ni}^{ol/liq}$ and $D_{Mg}^{ol/liq}$ is strong, both Jones (1984) and Beattie et al. (1991) acknowledge that a strict thermodynamic treatment of partitioning data using an exchange reaction leads to a linear relationship between $D_{Ni}^{ol/liq}$ and $D_{Mg}^{ol/liq}$ (with a y-intercept of zero), only if $\frac{\exp\left(-\Delta_{r(1)}G_{T,P}^{\circ} / RT\right)}{\left(\gamma_{NiSi_{0.5}O_2}^{ol}\gamma_{MgO}^{liq}\right) / \left(\gamma_{MgSi_{0.5}O_2}^{ol}\gamma_{NiO}^{liq}\right)}$ is constant. Our experiments suggest that this term is not constant because $\Delta_{r(1)}G_{T,P}^{\circ}$ is nonzero. This conclusion is corroborated by comparing the partitioning of Ni to that of other divalent cations (e.g., Ca, Mn, Fe, Co); using the Jones-Beattie model, most other divalent cations have y-intercepts near zero (i.e., Table 1 from Beattie et al. 1991), whereas the y-intercept for Ni is not only non-zero (–3.66), it is nearly an order of magnitude larger in an absolute sense than the next largest value, −0.385 (Co). By allowing a non-zero intercept, the fit ceases to be firmly rooted in thermodynamics and becomes a linear fit to an observed correlation. Such correlations are useful and can provide useful insights but, without a mechanistic framework to help us interpret the observations, it can be difficult to correctly identify the variables that drive an observed variation. This issue can be greatly magnified when the underlying data set has many cross-correlated variables. As we, and many others have observed, many variables (notably, temperature, composition, and $D_{Mg}^{ol/liq}$) in the database of available Ni-partitioning experiments are strongly correlated with one another (e.g., Arndt 1977; Hart and Davis 1978; Takahashi 1978; Matzen et al. 2013). Thus, we urge caution in using a Jones-Beattie type expression for olivine-liquid Ni partitioning when modeling a process such as high-pressure mantle partial melting followed by low-pressure crystallization. During such a process, temperature and $D_{Mg}^{ol/liq}$ may be decoupled.

Conditions of mantle melting and heterogeneity: Conclusions from Ni contents of olivines vs. bulk rock geochemistry

A significant finding of our work is that the temperature dependence of $D_{Ni}^{ol/liq}$ causes the formation of near-surface primitive olivine phenocrysts with NiO contents that should scale with thickness of the lithosphere through which they were erupted (assuming the temperature contrast between the mantle source and olivine saturation near the surface is controlled by lithospheric thickness). Our predictions compare favorably with the NiO contents of magnesian olivine phenocrysts, suggesting that variations in observed NiO contents may reflect melting of and equilibration with mantle peridotite under lithospheric lids of varying thickness. This finding appears to contrast with conclusions of Dasgupta et al. (2010) who, using the major-element thermobarometer of Lee et al. (2009), showed that, for a large fraction of island-averaged calculated primary melts, the mean pressure of melting was significantly deeper than the base of the lithosphere. There are several possible explanations for the apparent inconsistency but the most reasonable one is that, as discussed by Dasgupta et al. (2010), the calculated pressures of melting based on silica activity reflect mean melting pressures. The favored model of Dasgupta et al. (2010) posits a source region for OIBs that contains at least two components, one of which is peridotite—the additional component in low-silica alkaline OIB source regions is a carbonated eclogite; for “high-silica” OIB magmas like those erupted on Hawaii, the additional source component is volatile-free, silica-excess eclogite (i.e., subducted MORB). Since both of these basaltic components have solidus temperatures below that of fertile peridotite at high pressures (e.g., Pertermann and Hirschmann 2003; Lambart et al. 2009; Gerbode and Dasgupta 2010), the major-element composition of a primary magma represents the "average" of relatively deep partial melts from the basaltic component and shallower partial melts from the peridotite (arguably up to the lithosphere-asthenosphere boundary). However, a MORB-based basaltic component is expected to have a low bulk nickel content (Hofmann 1988; Gale et al. 2013), and thus, the NiO content of the parental magmas will be defined by lower pressure equilibration with and partial melting of the peridotite. This would lead to pressure estimates using the NiO contents of primitive olivines that are less than those based on silica activities.

References

Arndt NT (1977) Partitioning of nickel between olivine and ultrabasic and basic komatiite liquids. Year Book - Carnegie Institution of Washington (76):553–557

Beattie P, Ford C, Russell D (1991) Partition coefficients for olivine-melt and orthopyroxene-melt systems. Contrib Mineral Petrol 109:212–224

Dasgupta R, Jackson MG, Lee C-TA (2010) Major element chemistry of ocean island basalts — Conditions of mantle melting and heterogeneity of mantle source. Earth Planet Sci Lett 289:377–392

Gale A, Dalton CA, Langmuir CH, Su Y, Schilling J-G (2013) The mean composition of ocean ridge basalts. Geochem Geophys Geosys 14:489–518

Gee LL, Sack RO (1988) Experimental petrology of melilite nephelinites. J Petrol 29:1233–1255

Gerbode C, Dasgupta R (2010) Carbonate-fluxed melting of MORB-like pyroxenite at 2.9 GPa and genesis of HIMU ocean island basalts. J Petrol 51:2067–2088

Hart SR, Davis KE (1978) Nickel partitioning between olivine and silicate melt. Earth Planet Sci Lett 40:203–219

Herzberg C, Asimow PD, Ionov DA, Vidito C, Jackson MG, Geist D (2013) Nickel and helium evidence for melt above the core-mantle boundary. Nature 493:393–397

Herzberg C, Cabral RA, Jackson MG, Vidito C, Day JMD, Hauri EH (2014) Phantom Archean crust in Mangaia hotspot lavas and the meaning of heterogeneous mantle. Earth Planet Sci Lett 396:97–106

Hofmann AW (1988) Chemical differentiation of the Earth: the relationship between mantle, continental crust, and oceanic crust. Earth Planet Sci Lett 90:297–314

Hole MJ, Millett JM (2016) Controls of mantle potential temperature and lithospheric thickness on magmatism in the North Atlantic Igneous Province. J Petrol 57:417-436

Jones JH (1984) Temperature- and pressure-independent correlations of olivine/liquid partition coefficients and their application to trace element partitioning. Contrib Mineral Petrol 88:126–132

Lambart S, Laporte D, Schiano P (2009) An experimental study of pyroxenite partial melts at 1 and 1.5 GPa: Implications for the major-element composition of Mid-Ocean Ridge Basalts. Earth Planet Sci Lett 288:335–347

Larsen LM, Pedersen AK (2000) Processes in high-Mg, high-T magmas: Evidence from olivine, chromite and glass in Paleogene picrites from west Greenland. J Petrol 41:1071-1098

Lee C-TA, Luffi P, Plank T, Dalton H, Leeman WP (2009) Constraints on the depths and temperatures of basaltic magma generation on Earth and other terrestrial planets using new thermobarometers for mafic magmas. Earth Planet Sci Lett 279:20–33

Matzen AK, Baker MB, Beckett JR, Stolper EM (2011) Fe-Mg partitioning between olivine and high-magnesian melts and the nature of Hawaiian parental liquids. J Petrol 52:1243–1263

Matzen AK, Baker MB, Beckett JR, Stolper EM (2013) The temperature and pressure dependence of nickel partitioning between olivine and silicate melt. J Petrol 54:2521–2545

Pertermann M, Hirschmann MM (2003) Partial melting experiments on a MORB-like pyroxenite between 2 and 3 GPa: Constraints on the presence of pyroxenite in basalt source regions from solidus location and melting rate. J Geophys Res 108:2125

Takahashi E (1978) Partitioning of Ni^{2+}, Co^{2+}, Fe^{2+}, Mn^{2+} and Mg^{2+} between olivine and silicate melts: compositional dependence of partition coefficient. Geochim Cosmochim Acta 42:1829–1844

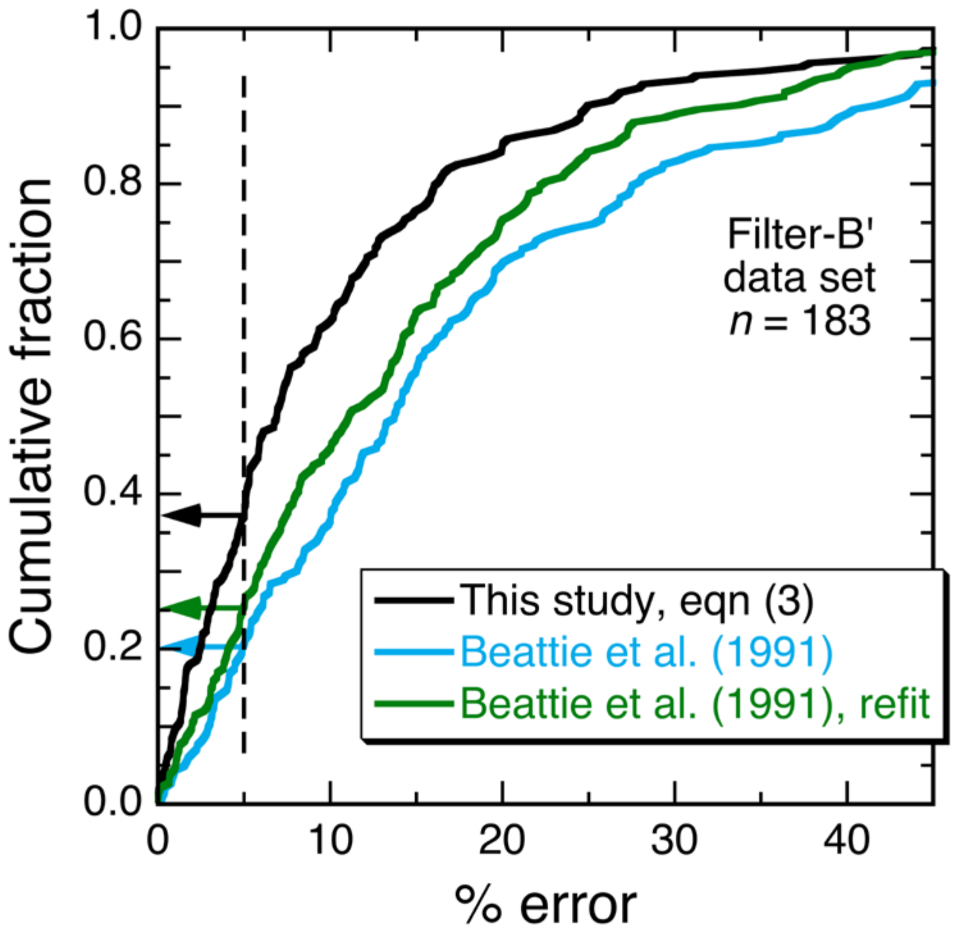

Fig. S1. Fraction of experiments whose relative percent errors ($100 \times \left| D^{ol/liq}_{Ni,calc} - D^{ol/liq}_{Ni,meas} \right| / D^{ol/liq}_{Ni,meas}$, where vertical bars denote absolute value and “calc” and “meas” refer to calculated and measured, respectively), are less than or equal to a given percent error. For each experiment in the Filter-B′ data set, $D^{ol/liq}_{Ni}$ s were calculated using the exchange reaction (3) fit to the Filter- B′ data set (black curve); the Jones (1984) and Beattie et al. (1991) equation ($D^{ol/liq}_{Ni} = \mathrm{A} \times D^{ol/liq}_{Mg} + \mathrm{B}$) and values for A and B from Beattie et al. (1991) (blue curve); and the same equation refit to the Filter-B′ data set (green curve). Horizontal arrows extend from each curve where it intersects a relative percent error of 5 (dashed line) and point to the fraction of the total number of experiments (*n* = 183) whose relative percent errors are ≤ 5. The thermodynamically-based exchange reaction (black curve) is better able to predict experimentally-measured $D^{ol/liq}_{Ni}$ s than a Jones-Beattie type model, despite both having the same number of free parameters.

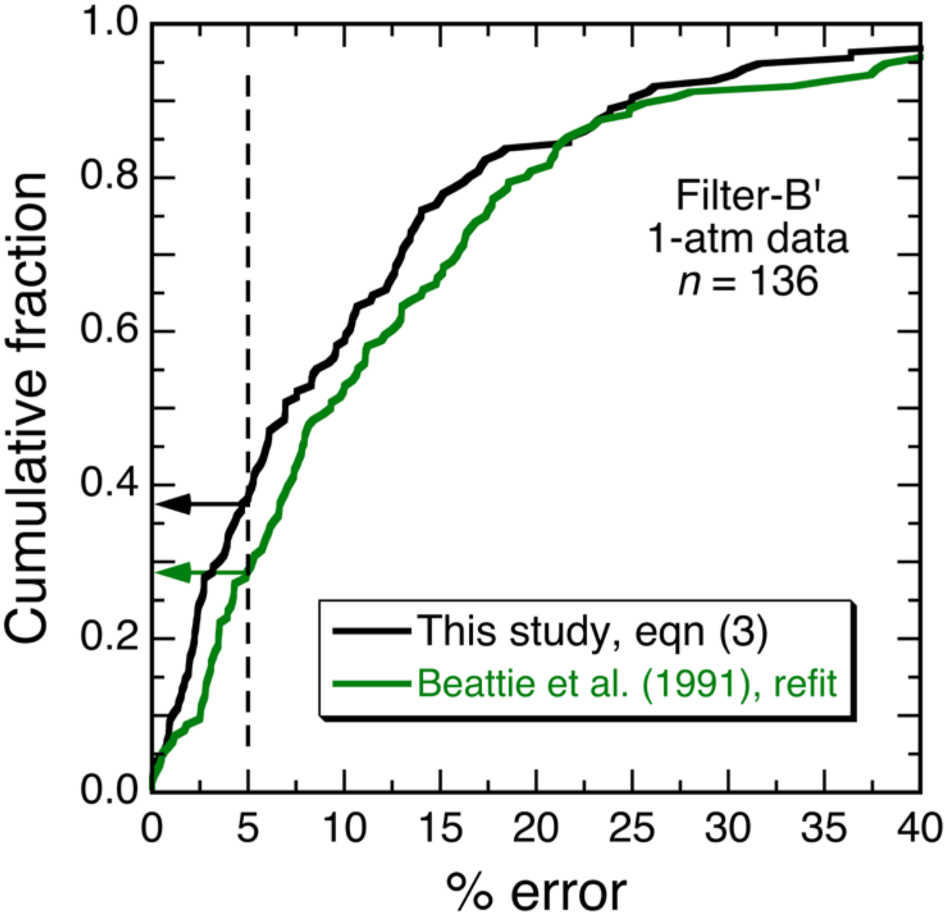

Fig. S2. Fraction of experiments whose relative percent errors, defined in the caption to Fig. S1, are less than or equal to a given percent error. For each 1-atm experiment in the Filter-B′ data set, $D_{Ni}^{ol/liq}$s were calculated using the exchange reaction (3) fit to the 1-atm experiments in the Filter-B′ data set (black curve) and the Jones (1984) and Beattie et al. (1991) equation ($D_{Ni}^{ol/liq}$ = A× $D_{Mg}^{ol/liq}$ + B) refit to the 1-atm Filter-B′ experiments (green curve). Horizontal arrows extend from each curve where it intersects a relative percent error of 5 (dashed line) and point to the fraction of the total number of experiments (n = 136) whose relative percent errors are ≤ 5.

Table S1

-XLS file

Table S2

-XLS file

Supplemental material to Matzen et al., The effect of liquid composition on the partitioning of Ni between olivine and silicate melt

Table S1. Estimated depths (km) to lithosphere-asthenosphere boundary (LAB), maximum observed ol Mg#, calculated ol NiO (wt. %) at maximum ol Mg#, and maximum observed ol NiO (w

Locality [a]	depth to LAB (km) [k]	rock type [p]	total number of samples	total number of analyses [q]	number of samples used in fit	number of analyses used in fit [x]	max ol Mg#	calc ol NiO at max ol Mg# [y]	± mean deviation	Fit	max ol NiO [z]	Mg# of ol with max NiO [bb]
MORB, Bouvet	0	thol	4	293	3 [r]	286	91.25	0.383	0.030	linear	0.452 [aa]	86.81
MORB, SEIR	0	thol	9	395	9	395	90.55	0.350	0.018	power law	0.352	90.11
MORB, Siqueiros FZ	0	thol	1	97	1	97	90.95	0.375	0.008	linear	0.380	90.95
MORB, FAMOUS	0	thol	3	294	3	294	91.85	0.343	0.023	linear	0.433	91.08
MORB, 9°N MAR	0	thol	2	146	2	146	90.08	0.330	0.017	linear	0.330	89.79
MORB, Garrett FZ	0	thol	1	107	1	107	91.09	0.368	0.024	linear	0.378	90.79
MORB, Romanche FZ	0	thol	12	501	12	467	90.58	0.285	0.014	power law	0.293	90.02
MORB, 43°N MAR (I) [b,c]	0	thol	8	569	5	466	91.77	0.313	0.017	linear	0.358	91.03
MORB, 43°N MAR (II) [b,d]	0	thol			3	101	90.28	0.349	0.005	linear	0.360	90.24
MORB, Knipovich ridge	0	thol	2	76	2	76	87.94	0.260	0.013	power law	0.246	87.58/87.45
H-E chain, Hawaii, Kilauea Iki	90.1	thol	3	246	3	246	89.00	0.437	0.010	power law	0.442	88.97
H-E chain, Hawaii, Mauna Loa, Puu Wahi	90.1	thol	1	119	1	119	89.04	0.409	0.012	power law	0.430	88.83
H-E chain, Hawaii, Mauna Loa HSDP2	90.1	thol	9	948	9	948	91.02	0.534	0.038	power law	0.603	90.06
H-E chain, Hawaii, Mauna Kea HSDP2	90.1	thol	42	3869	42	3869	90.99	0.485	0.022	power law	0.542	90.47
Hawaii, Mauna Kea, post-shield	90.1	thol	4	272	2 [s]	166	89.49	0.410	0.012	power law	0.438	89.14
H-E chain, Oahu, Koolau Makapuu	88.8 ± 0.1	thol	7	590	7	590	89.78	0.496	0.029	linear	0.593	89.48
H-E chain, Oahu, Koolau KSDP	88.8 ± 0.1	thol	1	107	1	107	89.46	0.470	0.012	linear	0.541	89.46
H-E chain, Loihi - tholeiites	90.1	thol	20	962	20	958	89.93	0.413	0.013	power law	0.424	88.21
H-E, Loihi - alkalic basalts	90.1	alkalic	2	192	2	192	90.21	0.451	0.014	power law	0.444	90.21
H-E chain, Detroit seamount	49.5 [l]	thol	2	126	2	126	90.42	0.419	0.013	power law	0.402	89.41
H-E chain, Suiko seamount	64.8 [l]	uncertain	2	66	2	66	89.06	0.448	0.014	linear	0.439	89.06
Iceland, Reykjanes (I) [b,e]	32.3 –7.2/+5.0	thol	5	287	3	189	91.28	0.358	0.011	linear	0.365	91.28
Iceland, Reykjanes (II) [b,f]	32.3 –7.2/+5.0	thol			2	98	89.09	0.309	0.014	linear	0.314	88.21
Iceland, Hengill, Midfell & Maelifell	32.3 –7.2/+5.0	thol	3	158	3	152	90.96	0.340	0.014	linear	0.376	90.91
Iceland, Kistufell	32.3 –7.2/+5.0	thol	4	205	4	203	89.62	0.332	0.008	linear	0.344	88.44
Iceland, Theistareykir (I) [b,g]	32.3 –7.2/+5.0	thol	8	454	5	241	91.09	0.343	0.011	linear	0.379	91.09
Iceland, Theistareykir (II) [b,h]	32.3 –7.2/+5.0	thol			4	209	90.37	0.370	0.011	linear	0.369	90.37
Iceland, Snaefellsnes (I) [b,i]	32.3 –7.2/+5.0	uncertain	3	218	1	100	89.65	0.319	0.008	linear	0.313	89.65/89.44
Iceland, Snaefellsnes (II) [b,j]	32.3 –7.2/+5.0	uncertain			2	105	89.66	0.283	0.012	linear	0.287	89.12/88.40
West Greenland	100 [m]	thol	6	284	6	284	92.68	0.484	0.017	linear	0.484	92.68
Baffin Island	65 [n]	thol	6	190	6	186	92.65	0.445	0.012	power law	0.446	92.35
Azores, Sao Migel	67.6	alkalic	6	725	6	725	90.27	0.374	0.018	power law	0.401	89.59
Azores, Terceria	47.2 ± 0.2	alkalic	2	268	2	268	89.40	0.362	0.012	power law	0.367	88.68
Canary Islands, Gran Canaria	96.1	alkalic	6	123	3 [t]	74	89.17	0.464	0.016	power law	0.473	89.17
Reunion	83.4 ± 0.1	thol & alkalic	3	301	3	301	90.08	0.394	0.006	linear	0.400	90.07
Galápagos, San Cristobal	35.5 –2.0/+1.8	uncertain	7	332	7	332	91.15	0.310	0.018	power law	0.298	88.65
Galápagos, Espanola	39.8 ± 0.1	alkalic?	1	59	1	59	87.10	0.245	0.010	power law	0.269	86.71
Galápagos, Santa Fe	33.7	thol	2	51	1 [u]	39	87.70	0.367	0.012	power law	0.364	87.53
Galápagos, Santa Cruz	36 ± 0.4	uncertain	11	571	1 [v]	55	88.07	0.348	0.009	linear	0.342	88.02
Galápagos, Floreana	42.1 ± 0.8	alkalic?	5	327	5	301	90.84	0.367	0.017	power law	0.336	88.60
Galápagos, Santiago	37.5 ± 0.5	uncertain	2	160	2	159	87.48	0.374	0.019	power law	0.371	87.48
Galápagos, Isabela, Volcan Ecuador	35.8 –4.5/+3.6	uncertain	3	113	3	113	87.62	0.378	0.013	power law	0.387	87.62
Galápagos, Isabela, Cerro Azul	35.8 –4.5/+3.6	thol	6	379	4 [w]	285	89.12	0.300	0.009	linear	0.309	89.12
Galápagos, Fernandina	37 [o]	thol & alkalic	10	552	10	552	88.78	0.311	0.017	linear	0.370	86.21

Notes to Table S1:

[a] Galapágos data from Vidito et al. (2013), West Greenland and Baffin Island/Bay data from Herzberg et al. (2016) and Soboleve et al. (2007), all other data from Sobolev et al. (2007), H-E = Hawaiian-Emperor chain; [b] Two relatively distinct populations of olivines are seen in plots of ol Mg# vs. ol NiO content; [c] (I) consists of olivine analyses from samples AII-32 11-178, 12-6, 11-92, 12-7, and 12-2; [d] (II) consists of olivine analyses from samples AII-32 12-6, 12-7, and AII-60; [e] (I) consists of samples 03-106, 03-102, and 01-7; [f] (II) consists of samples 01-15 and 01-12; [g] (I) consists of samples 01-55, 01-57-4, 01-56-1, 01-56-2; [h] (II) consists of sample: 01-57-4, 01-54, 01-44, 01-41; [i] (I) consists of sample 03-224; [j](II) consists of samples 03-226 and 03-220; [k] depth to the LAB bounday for MORBs assumed to be zero, other values, except where noted, are from Dasgupta et al. (2010) and refer to depth at the time of eruption, uncertainties are those listed in Dasgupta et al. (2010); [l] seamount and crustal ages from Keller et al. (2000), depths calculated based on polynomial fits to the Pacific data in Table 1 of Dasgupta et al. (2010); [m] Larsen and Pedersen (2000); [n] Hole and Millett (2016); [o] eruption ages are assumed to be young (Geist et al. 2006), depth to the LAB assumed to be similar to that of Santiago (Dasgupta et al. 2010); [p] thol = tholeiitic, uncertain means that the samples numbers could not be linked to specific rock compositions and that neither tholeiitic nor alkalic basalts in the Georoc database constituted more than 80% of the analyzed samples from the area in question, "?" following a designation indicates that 80 – 95% of the whole rock data were that rock type, no "?" means that either the sample numbers associated with the olivine analyses could be assigned to specific rock analyses or that >95% of the whole rock data ($SiO_2 \leqslant 54$ wt. % and $MgO \geqslant 6$ wt. %) were either tholeiitic or alkalic (based on Alkalinity Index, Rhodes and Vollinger, 2004); [q] includes all analyses for that suite/locality; [r] samples AG32, AG32-336, and B341; [s] samples KI-3 and KI-11; [t] samples 953C-93R-04, -05, and -06; [u] sample SF-7; [v] GFZ11; [w] samples CA-14, -16, -45B, and -53; [x] the number of analyses used to fit the linear or power law equations, clear outliers on plots of ol Mg# vs. ol NiO were excluded as were olivines with ≤0.15 wt. % CaO (except for Koolau Makapuu were the one low-CaO olivine analysis was retained; low-CaO olivines in Galapagos samples are widely interpreted as representing mantle xenocrysts, e.g., Vidito et al. 2013); [y] calculated using the regression equations (see Table S2) and the max olivine Mg#; [z] the maximum NiO content observed in those samples in a given suite/locality that were used to derive the linear or power law fits; [aa] although the CaO content of this olivine is >0.15, its value is still 5.6 standard deviations below the mean of this data set; [bb] two values indicate that the maximum NiO value was associated with two different olivine analyses

References:

Dasgupta et al. (2010) Earth Planet Sci Lett 289, 377-392

Geist et al. (2006) Geochem Geophys Geosys 7(12), 10.1029/2006GC001290

Hole and Millett (2016) J Petrol 57, 417-436

Keller et al. (2000) Nature 405, 673-676

Larsen and Pedersen (2000) J Petrol 41, 1071-1098

Rhodes & Vollinger (2004) Geochem Geophys Geosys 5(3), 10.1029/2002GC000434

Sobolev et al. (2007) Science 316, 412-417

Vidito et al. (2013) Geochem Geophys Geosys 10, 4214-4240

Supplemental material to Matzen et al., The effect of liquid composition on the partitioning of Ni between olivine and silicat

Table S2. Coefficients for the linear and power law equations used to calculate ol NiO at maximum ol Mg# [a]

Locality	Coefficients on linear fits		Coefficients on power law fits (NiO = a + b*[(Mg# ol)/100]ˆc)		
	slope	y-inter	a	b	c
MORB, Bouvet	0.06262	-5.3304			
MORB, SEIR			0.1135	4.1608	28.8735
MORB, Siqueiros FZ	0.06315	-5.3681			
MORB, FAMOUS	0.03902	-3.2414			
MORB, 9°N MAR	0.02572	-1.9862			
MORB, Garrett FZ	0.04238	-3.4922			
MORB, Romanche FZ			0.0353	0.6460	9.5940
MORB, 43°N MAR (I)	0.02002	-1.5240			
MORB, 43°N MAR (II)	0.05517	-4.6318			
MORB, Knipovich ridge			0.0563	35.4013	40.1368
H-E chain, Hawaii, Kilauea Iki			0.3153	120.4195	59.1791
H-E chain, Hawaii, Mauna Loa, Puu Wahi			0.2822	5.0848	31.7494
H-E chain, Hawaii, Mauna Loa HSDP2			0.2606	1.4996	18.0771
H-E chain, Hawaii, Mauna Kea HSDP2			0.1735	0.9232	11.5149
Hawaii, Mauna Kea, post-shield			0.2315	7.7268	33.9406
H-E chain, Oahu, Koolau Makapuu	0.02833	-2.0465			
H-E chain, Oahu, Koolau KSDP	0.02218	-1.5143			
H-E chain, Loihi - tholeiites			0.1649	0.8074	11.0960
H-E, Loihi - alkalic basalts			0.1600	3.0328	22.7342
H-E chain, Detroit seamount			0.1809	1.2689	16.5954
H-E chain, Suiko seamount	0.02658	-1.9185			
Iceland, Reykjanes (I)	0.03671	-2.9929			
Iceland, Reykjanes (II)	0.01914	-1.3963			
Iceland, Hengill, Midfell & Maelifell	0.02946	-2.3398			
Iceland, Kistufell	0.03335	-2.6569			
Iceland, Theistareykir (I)	0.03973	-3.2755			
Iceland, Theistareykir (II)	0.02916	-2.2653			
Iceland, Snaefellsnes (I)	0.03064	-2.4276			
Iceland, Snaefellsnes (II)	0.02256	-1.7395			
West Greenland	0.02176	-1.53276			
Baffin Island/Bay			0.1675	0.5884	9.8312
Azores, Sao Migel			0.1452	6.1129	32.1080
Azores, Terceria			0.0780	2.2882	18.6230
Canary Islands, Gran Canaria			0.2754	2.2486	21.6239
Reunion	0.02213	-1.5995			
Galápagos, San Cristobal			-0.0051	0.5184	5.3747
Galápagos, Espanola			0.0488	0.5806	7.8674
Galápagos, Santa Fe			0.1729	1.8744	17.2858
Galápagos, Santa Cruz	0.03851	-3.0429			
Galápagos, Floreana			0.0597	0.8193	10.1931
Galápagos, Santiago			0.0962	0.9275	9.0174
Galápagos, Isabela, Volcan Ecuador			-0.0175	1.9099	11.9084

Galápagos, Isabela, Cerro Azul	0.01778	-1.2849			
Galápagos, Fernandina	0.02212	-1.6521			

[a] Coefficents were calculated by minimizing the sum of the absolute deviations; olivine Mg# as defined in the main text, 100*Mg/(Mg+Fe), molar

te melt